applied sciences

MDPI

Article

Evaluating 3D-Printed Polylactic Acid (PLA)-Reinforced Materials: Mechanical Performance and Chemical Stability in Concrete Mediums

Hanna Csótár [1], Szabolcs Szalai [1], Dmytro Kurhan [2], Mykola Sysyn [3] and Szabolcs Fischer [1,*]

[1] Central Campus Győr, Széchenyi István University, H-9026 Győr, Hungary; csotar.hanna@sze.hu (H.C.); szalaisz@sze.hu (S.S.)
[2] Department of Transport Infrastructure, Ukrainian State University of Science and Technologies, UA-49005 Dnipro, Ukraine; d.m.kurhan@ust.edu.ua
[3] Department of Planning and Design of Railway Infrastructure, Technical University Dresden, D-01069 Dresden, Germany; mykola.sysyn@tu-dresden.de
* Correspondence: fischersz@sze.hu; Tel.: +36-(96)-503-400

Abstract: The optimization and evaluation of 3D-printed polylactic acid (PLA) materials for reinforcing concrete elements present a promising avenue for advancing sustainable construction methods. This study addresses the challenges associated with PLA's dual nature—biodegradable yet mechanically limited for long-term applications—while leveraging its potential to enhance concrete reinforcement. The research identifies gaps in understanding PLA's mechanical and chemical behavior in alkaline environments, particularly its interactions with concrete matrices. To bridge this gap, four distinct PLA variants (high-impact PLA, engineering PLA, electrical ESD PLA, and gypsum PLA) and ABS (acrylonitrile butadiene styrene) were subjected to dissolution tests in NaOH solutions (pH 12 and 12.55) and mechanical evaluation under three-point bending using digital image correlation (DIC) technology. Test specimens were prepared using optimized 3D printing strategies to ensure structural consistency and were embedded in concrete beams to analyze their reinforcement potential. Force–displacement data and GOM ARAMIS measurements revealed significant differences in mechanical responses, with peak loads ranging from 0.812 kN (high-impact PLA) to 1.021 kN (electrical ESD PLA). Notably, electrical ESD PLA exhibited post-failure load-bearing capacity, highlighting its reinforcement capability. Chemical dissolution tests revealed material-specific degradation patterns, with high-impact and Gypsum PLA showing accelerated surface changes and precipitation phenomena. Observations indicated white crystalline precipitates, likely lime (calcium hydroxide—$Ca(OH)_2$), residue from the dissolution tests (sodium hydroxide—NaOH), or material-derived residues formed on and near PLA elements, suggesting potential chemical interactions. These findings underline the critical role of material selection and optimization in achieving effective PLA–concrete integration. While PLA's environmental sustainability aligns with industry goals, its structural reliability under long-term exposure remains a challenge. The study concludes that electrical ESD PLA demonstrates the highest potential for application in reinforced concrete, provided its chemical stability is managed, as its peak value (1.021 kN) showed 25.7% higher load-bearing capacity than high-impact PLA (0.812 kN) and did not lose any of its structural stability in the dissolution tests. This work advances the understanding of PLA as a sustainable alternative in construction, offering insights for future material innovations and applications.

Keywords: sustainability; FDM; PLA; 3D-printed structures; glass-reinforced PLA; reinforced; concrete; DIC; GOM ARAMIS; GOM ATOS

Academic Editors: Raffaele Zinno, Eleni Tsangouri and Jiping Bai

Received: 29 November 2024
Revised: 7 February 2025
Accepted: 16 February 2025
Published: 18 February 2025

Citation: Csótár, H.; Szalai, S.; Kurhan, D.; Sysyn, M.; Fischer, S. Evaluating 3D-Printed Polylactic Acid (PLA)-Reinforced Materials: Mechanical Performance and Chemical Stability in Concrete Mediums. *Appl. Sci.* **2025**, *15*, 2165. https://doi.org/10.3390/app15042165

1. Introduction

The 21st century's engineering undoubtedly plays a prime role in the pursuit of the greatest human needs, incorporating many forms of engineering, such as civil [1–5], mechanical [6–9], electrical [10,11], vehicle engineering [12,13], transportation, logistics [14,15], cognitive mobility [16–20], and environmental and chemical engineering [21,22], towards the quest of sustainable development [23–26]. They are responsible for developing sustainable engineering systems, and civil engineering is responsible for addressing the infrastructural systems of present-day societies with highly resilient and environmentally friendly materials. Moreover, mechanical engineering develops systems and machines that require less energy to operate. Electrical engineering promotes the use of renewable energy systems and establishes smart grid networks, which include sustainable approaches to the supply of power. Moreover, vehicle and transportation engineering has advanced the mobility industry with the use of electric and self-driving vehicles and has reengineered logistics systems to be more efficient while reducing emissions. Environmental engineering stitches all these professional spheres together and ensures that various technological advances are made responsibly and with awareness of eco-friendly and sustainable global goals.

However, considering this interplay, there comes the integrated notion that for sustainability across these groups, there must be coalescence, integrating approaches that minimize wastage, protect resources, or optimize functionality, which logistics does by integrating transportation with energy and infrastructure to create an efficient supply chain that is also environmentally friendly. Developing strategies within these sectors positively impacts the environment while simultaneously strengthening economies, increasing urban sustainability, and enhancing the overall living experience. Such a multi-faceted strategy complements the goal of engineering in its continuous improvement and its commitment to the Sustainable Development Goals of the United Nations [27].

Out of these fields, 3D printing makes it possible for materials to be consumed over a greater volume. It makes construction, manufacturing, and transport mechanisms more and more efficient. Advocacy for 3D-printed parametric designs in concrete as a material in reinforced structures for sustainable housing is built in this work. Organizations can leverage these technologies to enhance engineering cross-disciplinarity by solving the challenge of materials' sustainability while increasing infrastructure resiliency and performance.

Three-dimensional printing is transforming construction by enabling precise, layer-by-layer manufacturing that reduces material waste and enhances sustainability [28–30]. This technology allows for customizable and scalable structures, optimizing resource use while minimizing environmental impact. Its adaptability supports the production of complex components, from small to large, with minimal waste, making it an efficient method for sustainable housing [31]. Additionally, it accelerates construction through rapid prototyping [32–34]. The printing table's volume determines object size, allowing for diverse component production [33,34].

Despite its advantages, additive manufacturing faces challenges, particularly with PLA (polylactic acid). PLA's dual nature—biodegradable but lacking long-term durability—raises concerns for industrial applications [35,36]. Its slow and undefined decomposition process complicates sustainable use [37,38]. Researchers have explored material blending to tailor PLA's properties. For example, combining PLA with polycaprolactone (PCL) enhances biodegradation, achieving significant CO_2 conversion in soil and composting environments [39–44]. Accelerated degradation tests confirm that temperature significantly affects PLA decay, influencing crystallization and surface damage [44].

PLA's physical limitations, including low thermal stability and high thermal expansion, hinder its suitability for long-term applications in construction [45]. Exposure to heat and moisture can cause rapid deterioration, making it unsuitable for critical structures like

bridges and foundations [45–47]. Its expansion coefficient mismatch with other materials also raises structural concerns [46–48]. Consequently, PLA is primarily used in applications where high thermal and moisture resistance are not required.

Despite these limitations, PLA is being investigated as a reinforcing material in concrete. Unlike its use in other fields, PLA in construction is incorporated to enhance mechanical properties rather than degrade [48–53]. Reinforcement effectiveness is assessed through laboratory tests and finite element modeling [54–60]. The arrangement of 3D-printed reinforcements significantly affects structural performance. Studies demonstrate that specific geometries, such as rhomboid and honeycomb patterns, improve strength and durability [61,62]. Additionally, incorporating small aggregates like steel fibers further enhances reinforcement [63,64].

Several studies highlight the potential of 3D-printed PLA for strengthening concrete. Integrating porous PLA structures into cement matrices significantly improves mechanical properties. For instance, schwarzite- and zeolite-based PLA structures were shown to increase specific elasticity by 128.1% and 505.33%, respectively [57]. Xu et al. [65] examined surface modifications on 3D-printed PLA reinforcement, demonstrating that coatings like epoxy resin and steel fiber-sprayed epoxy enhance flexural strength. Sand and steel fiber coatings improved mechanical properties, emphasizing the importance of surface treatments for performance optimization.

Based on the literature review in the present study, 3D printing offers customizability, minimal waste, and cost efficiency, making it a valuable tool for construction. However, PLA's thermal and hydrolytic instability limit its use in demanding environments. Research shows that PLA can reinforce concrete under specific conditions, compensating for its limitations. While PLA degradation has been extensively studied, its solubility parameters in different solvents require further standardization. This research investigates the mechanical and chemical behavior of PLA variants and ABS in concrete, evaluating their reinforcement potential. Electrical ESD PLA demonstrated the highest reinforcement capability, exhibiting a 25.7% higher load-bearing capacity than high-impact PLA and retaining structural stability in dissolution tests. These findings contribute to the development of sustainable, high-performance construction materials.

This paper focuses on reinforcing concrete beams with 3D-printed PLA structures and is a continuation of a previous publication [66]. As in the previous publication, the different uses of ECO PLA (printed in different forms and as a waste aggregate from printing waste) are presented. In this paper, the authors focused on the diversity of different materials and their effects on mechanical load-bearing capacity and chemical stability in an experimental simulated environment.

The primary objective of this research is to investigate the behavior of various materials in the concrete medium, focusing on their reinforcement potential, solubility in NaOH solutions with pH levels similar to concrete, and performance under mechanical loading. The study examines five materials commonly used in engineering fields—PLA (high-impact, engineering, electrical ESD, and gypsum) and ABS (see Sections 2 and 3)—each selected for its distinct mechanical properties, compatibility with different 3D-printing strategies, and applications in industries such as electronics, automotive, modeling, and robotics.

ABS, in particular, was chosen for its high impact resistance, stiffness, and recyclability, making it a relevant candidate for innovative reinforcement strategies; however, the most relevant reason for the consideration was the fact that ABS is the most common base material for 3D printing in engineering; so, ABS was the benchmark material for appropriate consideration with PLA types. Three-dimensional printing with ABS filaments is usually "complicated" and problematic. In contrast, PLA has been developing very dynamically in

recent years, especially PLA composites. Its printability is also better, as is its environmental impact. PLA was investigated precisely as an alternative to ABS.

The study evaluates the potential of these materials as sustainable alternatives to conventional concrete reinforcements like steel and Kevlar. However, the primary focus lies in understanding the chemical reactions and solubility of these materials in NaOH solutions as well as their resistance under three-point mechanical loading tests.

While this research was limited to five materials due to constraints, it lays the groundwork for future studies that will explore additional options, such as PET-G (polyethylene terephthalate glycol-modified) and PCTG (polycyclo-hexylenedimethylene terephthalate glycol-modified). The structure of the study includes the following sections: Section 1 is the Introduction, Section 2 contains Materials and Methods, Section 3 introduces Results and Discussion, and Section 4 presents Conclusions.

The main contributions of the paper are as follows:

- Exploring 3D-printed PLA and ABS for concrete reinforcement—the study investigates the use of 3D-printed structures as an alternative reinforcement material for concrete beams, continuing previous research on PLA applications [66];
- Comparative analysis of engineering materials—it examines the performance of five engineering materials (high-impact PLA, engineering PLA, electrical ESD PLA, gypsum PLA, and ABS) in a concrete environment, focusing on mechanical load-bearing capacity and chemical stability;
- ABS as a benchmark for PLA—ABS is used as a benchmark due to its widespread use in 3D printing and its mechanical properties. The study evaluates PLA as a potential alternative to ABS, emphasizing PLA composites' advantages in printability and environmental impact, as ABS is non-degradable (see Section 2.1);
- Chemical and mechanical testing—investigation of the solubility of the material in NaOH solutions (simulating the high-pH environment of concrete) and the mechanical resistance using three-point bending tests;
- Sustainability and future research directions—these highlight the potential of PLA and other materials as sustainable replacements for conventional reinforcements like steel and Kevlar. The study also paves the way for future investigations, suggesting further research on materials like PET-G and PCTG.

2. Materials and Methods

In order to provide a better understanding of the paper and its results, a flowchart is provided (Figure 1) so that the reader can fully understand the two parallel measurements.

2.1. Applied PLA Materials (Filaments)

First of all, the authors should mention that the applied and considered materials were chosen for the following reasons:

- ABS was chosen as a benchmark material due to its widespread use in 3D printing for engineering, high impact resistance, stiffness, and recyclability;
- PLA was investigated as a dynamic and eco-friendly alternative to ABS, with superior printability and lower environmental impact;
- ABS, despite its ordinary use, presents challenges in 3D printing, while PLA composites have shown significant advancements in recent years;
- The inclusion of both ABS and PLA allows for a comparative analysis of their properties, environmental impact, and printing requirements;
- The study emphasizes sustainability and material optimization, aligning with the goal of advancing eco-friendly construction methods;

- While PLA offers environmental benefits, its limitations in specific applications are acknowledged, highlighting the need for balanced material selection in 3D-printed concrete reinforcement.

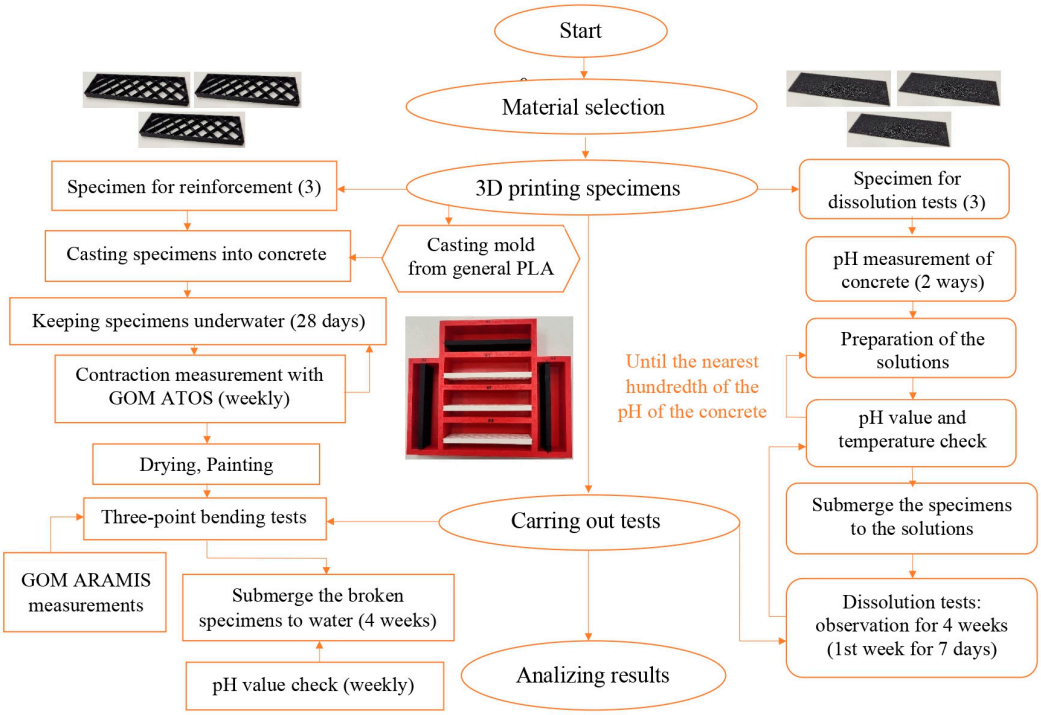

Figure 1. Flowchart of the measurements and methods.

During the tests, five different types of PLA material were used. High-impact PLA provides a higher impact resistance to the structure than PETG (polyethylene terephthalate glycol) materials and has a similar flexibility to polypropylene (PP).

Engineering PLA was selected because the heat resistance of printed objects is exceptionally high, withstanding temperatures of up to 120 °C, which can be achieved without the need for post-heat treatment. This makes it much more resistant to external influences than other PLA materials. It also has high tensile and compressive strength and extremely high stiffness.

The next material to be selected was electrical ESD (electrostatic discharge) PLA, which is a fiber-printed object that does not charge electrostatically due to special carbon and chemical additives. In addition, dust and fine dirt do not adhere to the surface of the objects. It provides a surface resistivity of the order of megaohms, but this depends mainly on the size and shape of the printed object. Furthermore, if printed at a higher temperature, it will provide a lower surface resistance. The surface resistance also depends on the print orientation, with a higher value in the *Z* direction and a lower value in the *XY* direction.

The following material is slightly different from the other ones. While other materials are generally used in the automotive and electronics industries, gypsum PLA is the preferred product for modeling due to its high formability. Objects printed with gypsum PLA are very easy to shape, as they can be cut and filed with a sharp tool, making it easier to machine the object afterward. Painting is also easy, even with water-based paints.

The last material used for sample and reinforcement production was ABS (acrylonitrile butadiene styrene), a widely used thermoplastic in the automotive, electronics, and engineering industries, valued for its high impact resistance and stiffness. While more challenging to print than PLA, ABS offers low shrinkage and allows for fast, precise processing in 3D printing, making it well suited for research. Its behavior in concrete—for instance, its

solubility in NaOH solution simulating the pH of concrete—provides valuable insights for developing sustainable and innovative reinforcement strategies. These qualities make ABS an ideal choice for this study, aimed at exploring new reinforcement solutions.

The casting molds were made from generic PLA, as they were designed to be single-use and needed to be quick and easy to dismantle. A total of six different materials were used during 3D printing, of which generic PLA was used only for the mold, and the other five materials were used for the test specimens. Furthermore, its solubility in NaOH solutions offers critical insights into its interaction with concrete media, contributing to sustainable and alternative reinforcement strategies. Table 1 represents the materials used and the recommended and applied printing parameters of the specimens.

Table 1. Recommended and used printing parameters of the specimens and molds.

Material	Mark	Manufacturer	Printing Parameters	Recommended [°C]	Applied [°C]
PLA	none	Filaticum Kft., Miskolc, Hungary	Nozzle temperature Bed temperature	190–215 55–70	200 60
High-impact PLA	HI	Filaticum Kft., Miskolc, Hungary	Nozzle temperature Bed temperature	190–210 45–65	200 60
Engineering PLA	ENG	Filaticum Kft., Miskolc, Hungary	Nozzle temperature Bed temperature	215–240 65–75	225 75
Electrostatic discharge PLA	ESD	Filaticum Kft., Miskolc, Hungary	Nozzle temperature Bed temperature	195–215 55–70	200 65
Gypsum PLA	GYP	Filaticum Kft., Miskolc, Hungary	Nozzle temperature Bed temperature	190–215 55–70	200 60
ABS	ABS	Filaticum Kft., Miskolc, Hungary	Nozzle temperature Bed temperature	260–290 80–95	260 90

The specimens were printed using the Creality Ender 3—v2 (Creality 3D Technology Co, Ltd., Shenzhen, China) 3D printer. The molds were printed with a Bambu Lab A1 (Bambu Lab, Shenzhen, China) mini printer.

However, the nozzle and bed temperature parameters applied differed according to the material; the other parameters, such as cooling rate, nozzle size, layer height, and printing speed, were the same. The applied identical printing parameters were as follows: nozzle size 0.4 mm, cooling fun 100%, layer height 0.2 mm, print speed 50 mm/s, and a skirt was also used.

Table 2 summarizes the materials tested (PLA, ABS, HI, ENG, and ESD) and compares their properties with each other and with other relevant materials (PETG); it also includes symbols for easy comparison.

Table 2. Comparative table of material properties.

Material	Tensile Strength	Flexibility	Heat Resistance [°C]	Printability	Eco-Friendliness
PLA	Moderate	Brittle	55–70	Easy	Biodegradable, non-recyclable
	••	••	•	•••	
HI	Moderate	Flexible	65–70	Easy	Biodegradable, non-recyclable
	••	••	••	•••	
ENG	High	Flexible	65–70	Easy	Biodegradable, non-recyclable
	•••	••	•••	•••	

Table 2. *Cont.*

Material	Tensile Strength	Flexibility	Heat Resistance [°C]	Printability	Eco-Friendliness
ESD	Moderate	Flexible	65–70	Moderately easy	Non-degradable
	••	••	••	••	
GYP	Low	Brittle	55–70	Easy	Biodegradable, non-recyclable
	•	·	•	•••	
ABS	Moderate	Flexible	80–95	Moderately hard	Non-degradable, recyclable
	••	••	•••	•	
PETG (polyethylene terephthalate glycol-modified PLA)	Moderate	Flexible	70–85	Easy	Non-degradable, recyclable
	••	•••	••	•••	

2.2. Applied Printing Set-Ups and Structures

Two different printing strategies were applied, as the research examines the relationship between PLA and concrete from two perspectives. The design was created using Solidworks 2016 × 64 Edition SP01 (SolidWorks Corporation, Waltham, MA, USA). To convert the stl. files to printing instructions, a slicing software, UltiMaker Cura 5.3 0 (Ultimaker, Geldermalsen, The Netherlands), was used.

The first layout concerned determining the solubility of the PLA material, so a 0.4 mm thick layer of sample was needed. During the printing process, the infill value did not influence the final structure of the PLA thin sheets due to its thin design. The size of the thin sample sheets was 25.0 × 0.4 × 80.0 mm.

The other layout was the structure, which was used as a reinforcing element in concrete beams, with a size of 25.0 × 5 × 80.0 mm. Each element was printed with a grid infill pattern and 10% infill density, with the top and bottom layers set to 0. As the initial and final layers were set to 0, the grid structure was visible.

This was a practical set-up as well as a functional one. Upon removing the initial and final layers, the printing time was reduced; furthermore, it was functional because, during casting, the concrete could spread between the gaps of the grid infill structure. Figure 2 shows the two structures in the UltiMaker Cura software with a coordinate system, and Figure 3 illustrates the six-cavity mold that was used during the casting of the concrete beams.

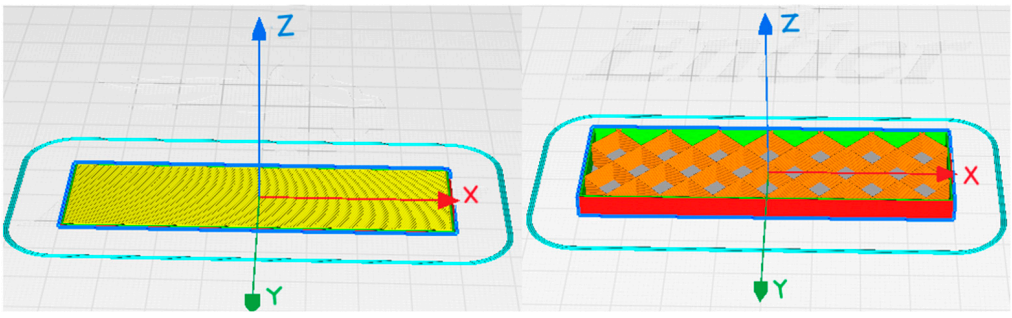

Figure 2. Printing set up of the specimens in UltiMaker Cura.

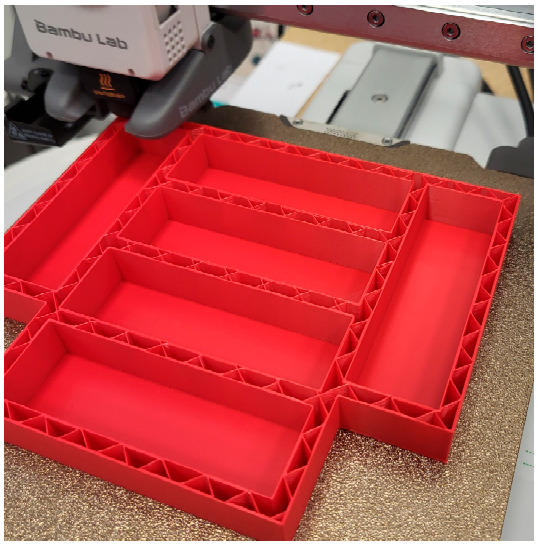

Figure 3. The structure of the PLA six-cavity mold.

The other printed (Figure 3) structure was the casting mold. The size of the concrete elements was 25.0 × 25.0 × 80.0 mm, so the inner size of the mold was identical. Three layers of the base were applied to the structure while printing. The wall thickness of the shape was 0.5 mm, with the same grid pattern and infill rate as the reinforcing element.

In summary, three and three samples were made per material: for each material, three were reinforcing elements for casting, and three were used for dissolution tests.

2.3. Molding Parameters

After the preparations of the printed elements, the casting of the reinforced concrete beams took place. The size of each concrete element was 25.0 × 25.0 × 80.0 mm (in accordance with the standard MSZ EN 12390-1:2021 [67]). The 3D-printed reinforcing elements were placed, for practical reasons, in the lower one-third of the mold prior to casting. The reinforcing element had to be close to the edge (bottom), far from the neutral axis, to provide a reinforcing effect, if any. (Particularly, its investigation was one of the main objectives of the current paper.) Figure 4 shows the location of the reinforcing material cast into concrete, and Table 3 represents the formula of the production for 1.6 L of concrete.

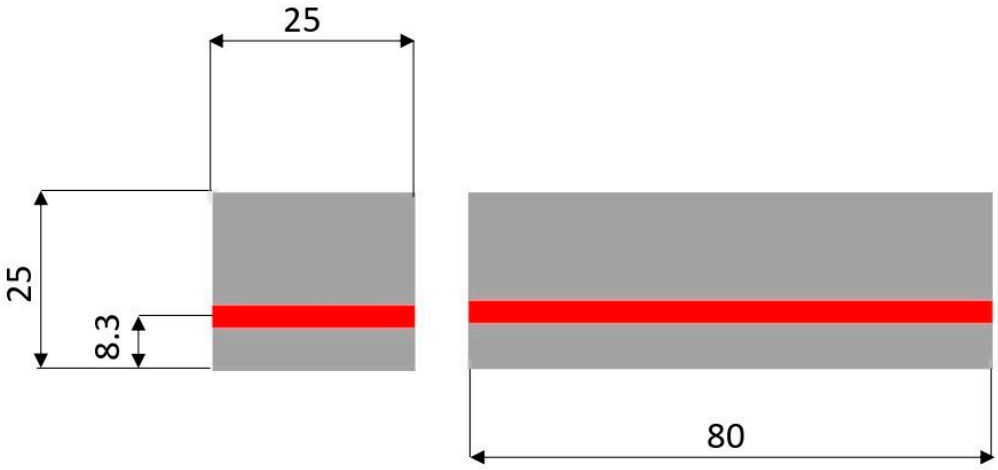

Figure 4. Location of the reinforcement in the concrete beam (units are in mm); L = 80 mm, d = 25 mm.

Table 3. Concrete composition per 1.6 L of concrete.

Material	Manufacturer (Brand)	Amount/Quantity
Water	-	480.6 g
Cement	CEM-II-AS-42.5 (Duna-Dráva Cement, Vác, Hungary)	1369.6 g
Limestone powder	Lafarge (Lafarge, Paris, France)	328.4 g
Fine aggregate	graded sand 0/1 (Duna-Dráva Cement, Vác, Hungary)	1489.8 g
Fluxing agent	VC 5 NEW (Sika, Baar, Switzerland)	8.8 mL

In order to yield a high-quality surface finish, which was needed for the GOM measurements, a Sica Separol AR-2 ECO-type (Sika Hungária Kft., Biatorbágy, Hungary) release agent was applied to the inside part of the mold before casting. After the preparation of the mold, the 3D-printed grid structures were placed in the mold, followed by the casting of the concrete. The next step was to remove the air trapped inside the mold using a Matest C278 vibro table (Matest, Treviolo, Italy).

The reinforcement was a 25.0 × 5 × 80.0 mm element with a structure predetermined by multiplying the sizes to obtain the volume, which was 10 cm^3. The concrete element without reinforcement weighed 114.88 g. The actual filled volume of the reinforcement with 10% infill was the volume multiplied by the percentage of the infill value, which was 1 cm^3, which means the percentage by volume for all substances was the same at 2%. Since the density of the reinforcing materials used is known, the volume and mass percentages of the elements can be calculated and are summarized in Table 4.

Table 4. Basic parameters of reinforced concrete elements.

Material	Mass [g]	Mass Percentage [%]	Volume Percentage [%]
ESD	1.24	1.07	2.0
ENG	1.24	1.07	2.0
HI	1.24	1.07	2.0
GYP	N/A	N/A	2.0
ABS	1.05	0.91	2.0

Table 4 shows that the mass and impact of the grid element on the concrete element remained minimal, especially for low infill and lower-density materials such as ABS. Following this analysis, the casting process proceeded to its final stage. After the solidification of the concrete elements, which took 24 h in the mold (in accordance with the standard MSZ EN 12390-2:2019 [68]), the elements were kept underwater for 27 more days to allow the inner solidification process of the concrete beams to finish. The underwater treatment of the test specimens resulted in a better-quality surface finish. The absence of surface cracks and surface defects facilitated the preparation of DIC measurements.

2.4. Bending Tests and DIC Measurements

The three-point bending tests were carried out with Zwick 1454 (Zwick Roell Group, US, Singapore) at 7.6 mm/min loading speed with load cell HBM U3 20 kN (HBM Ltd., Budapest, Hungary) and data collector HBM quantum MX840A (HBM Ltd., Budapest, Hungary), where the specimens were under load until they showed a sign of cracking. During the tests, a specific test method was applied rather than a standard one, where each test piece was loaded at 7.6 mm/min loading speed with load cell HBM U3 20 kN. A uniform load with a constant 20 kN causes the test specimens to move.

The amplification effect of the reinforcing elements can be determined as a function of the displacement of the test pieces relative to their initial state (vertical displacement in mm) and the resistance to the load (force in kN). The load was placed in the middle of the specimens, and the distance between the supports (i.e., bay length) was 75 mm. The tests were carried

out according to the MSZ EN 12390-5:2019 standard [69]. Since the laboratory we used is not an accredited measuring laboratory, and the measurement is related to research, the chosen length of L = 80 mm was used instead of the length $L \geq 3.5 \times d$ (87.5 mm), defined in MSZ EN 12390-5:2019 [69], where d is the dimension of the specimen in cross-section (i.e., the width and the height), as well as the distance between the support points and the applied vertical concentrated forces and between the two concentrated forces in the case of 4-point bending (see Figure 4).

In the case of the bending tests, even though the standard MSZ EN 12390-5:2019 [69] was included, the authors had to deviate from the instantaneous measurement described in the standard. The reason was the GOM ARAMIS (GOM, Braunschweig, Germany) measurements. It was necessary to deviate because if the paint had not adhered to the surface, the measurements would not have been able to be made since the technology calculates the amount of deformation from the displacements of the points painted on the surface.

Before laboratory experiments, each sample was dried for two days to ensure that moisture content did not affect the results. This was verified by weighing the specimens every 4 h on the first day and every hour on the second day until the difference in weight was negligible.

The specimens were then painted, first with a matte white lacquer primer (Deco Color Moto Techno Aerosol (Chemmot Ewa Kumorek Spółka Komandytowa, Skawina, Poland)) and then with a matte black lacquer topcoat spray (United Sealants Sprays Matte Black Spray (Neosil Kft., Bag, Hungary)).

Getting the paint pattern right was essential for the DIC (digital image correlation) GOM ARAMIS (GOM, Braunschweig, Germany) measurements. The issue of stain pattern was most carefully examined by Philipp Reu [70,71]. According to Reu, the pattern can be described by four primary characteristics: spot size, contrast, overlap of spots, and density of spots.

It is the combination of these characteristics that most accurately determines the spot size. The spot size is defined by the relationship between the resolution of the DIC camera system and the size of the sample area under inspection. These two data are used to calculate the size of the pixels in millimeters, with an optimum value of between 3 and 5 pixels. Smaller pixels are more difficult to detect during digitalization.

In addition, the overlap of speckles is a critical factor since if the speckle pattern overlap is not sufficient, images may become noisy during digitalization. For this reason, it is imperative to avoid overlapping when using speckle patterns, as this can negatively affect the measurement results.

The ability to identify displacements and deformations down to tenths of a millimeter with sufficient accuracy can enable the results to be used in a broader range of applications, whether in forensic, automotive, textile, or medical orthopedic applications [72].

Since light and surface reflectivity affect the camera's performance, the metallic, reflective areas were covered with masking tape to prevent interference with the measurement results. Figure 5 illustrates the experimental set-up and an appropriately painted surface that the measurement system recognizes so that it can be evaluated later.

The results were then evaluated using the GOM DIC ARAMIS 2018 (GOM, Braunschweig, Germany) evaluation software. The displacement data from the GOM system were then synchronized with the mechanical load values of the load cell, which are presented in Section 3.

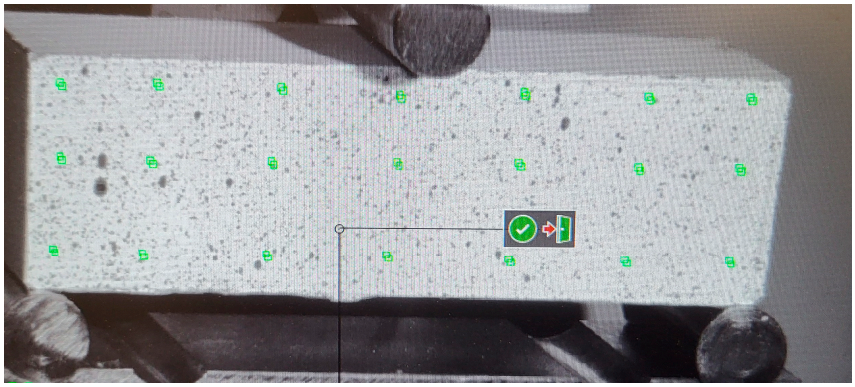

Figure 5. Experimental set-up with an appropriately painted surface, recognizable for the system.

Before starting the measurement, the camera was turned 180 degrees from its original position so that the coordinate system was also placed upside down, and the results were evaluated. The data were collected in parallel using the GOM ARAMIS (GOM, Braunschweig, Germany) camera system to measure displacement in the x direction and the HBM quantum MX840A (HBM, Darmstadt, Germany) data collector to record both force and displacement values.

The ARAMIS sampling frequency was 8 Hz, and the HBM sampling frequency was 10 Hz. During the evaluation, the ARAMIS displacement values and HBM force data were evaluated during the measurements. However, due to the different sampling frequencies, the data lengths were different, so a linear interpolation of the displacement values in the x direction of the GOM measurements was necessary based on the HBM force measurement data series size (see Section 3.1).

Besides the displacement measurements, the specimens were observed by GOM ATOS Triple Scan (GOM, Braunschweig, Germany) during the 28-day drying cycle to compare the stages of changes of the specimens. This differs from other technologies in that a painting process is not required in this case. Here, reference points with factory markings can be applied to the surface painted matte white.

Then, by adjusting the point size and temperature (object heat) of the camera, the machine scanned the surface by rotating the rotary table. This paper used a similar method as Szalai et al. [73], where a non-destructive diagnostic system (GOM) was used to more accurately identify potentially deformable areas during the adaptation of automotive batteries. In both cases, the measurement process was, of course, preceded by accurate and appropriate calibration requested and recommended by the manufacturer of the instruments.

2.5. Solvent Preparation and Tests

This section describes the parameters of the solvent compositions required for the experiments since the solubility of the PLA materials is another important point of this research. According to the factory descriptions, none of the tested materials are water soluble; only ABS has a defined solvent (THF—tetrahydrofuran acetone and other analogous solvents); the solubility of the other tested materials is not defined.

To carry out the tests, it was necessary to determine the pH of the concrete used, but there are several standards and methods for determining the pH of fresh concrete. pH is an approximate measure of the acidity or alkalinity of a solution, defined as the negative logarithm of the concentration of hydrogen ions (H^+).

As the pH of the solution increases, the number of free hydrogen ions decreases, and each unit increase in pH represents a tenfold decrease in H^+ concentration. The pH scale ranges from 0 to 14, where a pH of 7 is considered neutral; a pH below 7 indicates an acidic environment, while a pH above 7 indicates an alkaline environment.

The following examples show the relationship between H+ concentration and pH for different solutions:

- HCl (hydrogen chloride) solution, with an H^+ concentration of 1×10^{-2} and pH 2;
- H_2O (water), with an H^+ concentration of 1×10^{-7} and pH 7;
- Saturated $Ca(OH)_2$ (calcium chloride), with an H^+ concentration of $1 \times 10^{-12.4}$ and pH 12.4;
- NaOH (sodium hydroxide) solution, with an H^+ concentration of 1×10^{-14} and pH 14.

Grubb et al. [74] recognized the challenges and difficulties of the measurement of the pH value of concrete, reviewed the standard procedures, and recommended a test procedure. To measure the pH of solid materials such as lime, soil, or concrete, an aqueous solution of the powdered material must be created; this dilutes the concentration of the solid material.

Measurements were made with both a pH strip (i.e., so-called pH "paper") and a pH probe, following the steps suggested by [74] in the field test for pH measurement for concrete surface and laboratory test for pH measurement of concrete sections, with one amendment, i.e., using a sieve (size: 0.25 mm), since the authors of the current study had metric tools at their disposal [74].

The pH values were measured in two separate measurements. First, the pH of the fresh concrete was measured, followed by a laboratory pH test of the powder sample extracted from the reference test specimens, which had been dry for 28 days. Then, the pH of the freshly mixed concrete was measured, which was 12. This procedure was carried out using only pH test paper since the probe can only measure filtered solutions. The second measurement was a laboratory pH test.

Before the pH measurements were started, a water–concrete mixture of the correct proportions had to be prepared. The finely graded powder sample, taken from reference test specimens and kept dry for 28 days, was filtered with a 0.25 mm sieve, and then, the water–concrete mixture was prepared with a ratio of 10 mL to 5 g.

During the pH measurement series, ionized water of quality class 3 of MSZ ISO 3696:1992 [75] was used. (It has to be mentioned that this standard is a withdrawn standard, but the content as well as the methodology are still valid—theoretically.) Before measuring the pH, the solution was left to stand for 30 min, stirring occasionally, followed by 1.2 µm filtering. Then, the pH measurement was carried out using a WTW 720 pH meter (AKTIVIT Kft., Weilheim, Germany) and pH test paper (Cloud Prime, Seattle, WA, USA).

The pH measured with a pH meter was 12.55 (water–concrete mixture), and the pH measured with pH test paper (water–concrete mixture and fresh concrete) was 12, in both cases at 22.2 °C.

Since five different materials were tested (HI, ENG, ESD, GYP, and ABS), and three specimens were prepared per material, the amount of the solutions was determined accordingly. After determining the pH values, two solutions were prepared with NaOH powder. A 250 mL solution with pH 12.55 and a 500 mL solution with pH 12 were prepared.

Based on the previous measurements, two solutions were made, one with a pH value of 12 and one with 12.55, since the values of the pH strip measurement were identical.

The first solution was prepared from a mixture of 0.2 g NaOH powder and 500 mL ionized water and the second solution from a mixture of 0.355 g NaOH powder and 250 mL ionized water.

Equations (1)–(4) show the calculations for the first solution (500 mL) preparation (where M_{NaOH} = 40.00 g/mol, the pH value of the NaOH solution is 12, and the pH of the powdered NaOH solvent is 14):

$$pOH1 = 14 - 12 = 2 \quad (1)$$

$$[OH^-]_1 = 10^{-pOH1} = 10^{-2}\ [mol/L] = 0.01\ [mol/L] \quad (2)$$

$$n_1 = 0.01\ [mol/L] \times 0.5\ [L] = 0.005\ [mol] \quad (3)$$

$$m_1 = 40.00\ [g/mol] \times 0.005\ [mol] = 0.2\ [g] \quad (4)$$

Equations (5)–(8) show the calculations for the second solution (250 mL) preparation (where M_{NaOH} = 40.00 g/mol, the pH value of the NaOH solution is 12.55, and the pH of the powdered NaOH solvent is 14):

$$pOH2 = 14 - 12.55 = 1.45 \quad (5)$$

$$[OH^-]_2 = 10^{-pOH2} = 10^{-1.45}\ [mol/L] = 3.55 \times 10^{-2}\ [mol/L] \quad (6)$$

$$n_2 = 3.55 \times 10^{-2}\ [mol/L] \times 0.25\ [L] = 8.88 \times 10^{-3}\ [mol] \quad (7)$$

$$m_2 = 40.00\ [g/mol] \times 8.88 \times 10^{-3}\ [mol] = 0.355\ [g] \quad (8)$$

The solutions were mixed in several steps. First, the solutes were weighed on an analytical balance of hundredths accuracy. This was followed by a preliminary dissolution, where about two-thirds of the total solvent was added to the solute. After the exothermic reaction, the solution was diluted to the appropriate amount, and finally, after stirring, the pH value was adjusted with the pH meter to the nearest hundredth of the pH of the concrete until it was set to a predetermined value of 12 and 12.55.

After the preparations, the solutions were divided into five parts for 250 mL of pH 12.55 and ten parts for 500 mL of pH 12, so that 50 mL of solution was in measuring cups. Then, the 0.4 mm thin PLA samples were put into the solution and checked periodically after every 24 h for 28 days.

With this experiment, the aim was to observe the behavior of PLA and ABS specimens with a size of 25.0 × 0.4 × 80.0 mm in an alkaline medium with the same pH as the concrete over the same time interval as the concrete curing time.

3. Results and Discussion

This section describes in detail the observations collected during the experiments and the results obtained. The aim is to provide a comprehensive picture of the phenomena observed during the experimental process, the measurement data, and the relationships and conclusions that emerged during the investigation. Visual inspection tests, while preliminary, revealed significant qualitative insights into material behavior and surface interactions. These observations informed the design of supplementary tests, such as flame tests and pH evaluations, which provided quantifiable data to support and validate the visual observations. For instance, partial dissolution and discoloration phenomena in ABS and GYP samples highlighted complex interactions with the alkaline medium, paving the way for future detailed chemical characterization.

The analysis of the results is presented in Section 4. It enables a deeper understanding of the phenomenon under study and the identification of new relationships that can contribute to the further development of the research area.

3.1. Concerning the Mechanical Test and GOM ARAMIS Measurement Series

The mechanical properties of the test specimens were determined by plotting the force–displacement diagrams, which were determined using the GOM ARAMIS camera and HBM data collector systems.

Since the data from the two data collection and measurement systems were not linked, they had to be synchronized and matched later during the evaluation.

Figure 6 illustrates the force–displacement diagrams of the specimens, including the reference specimen without reinforcement.

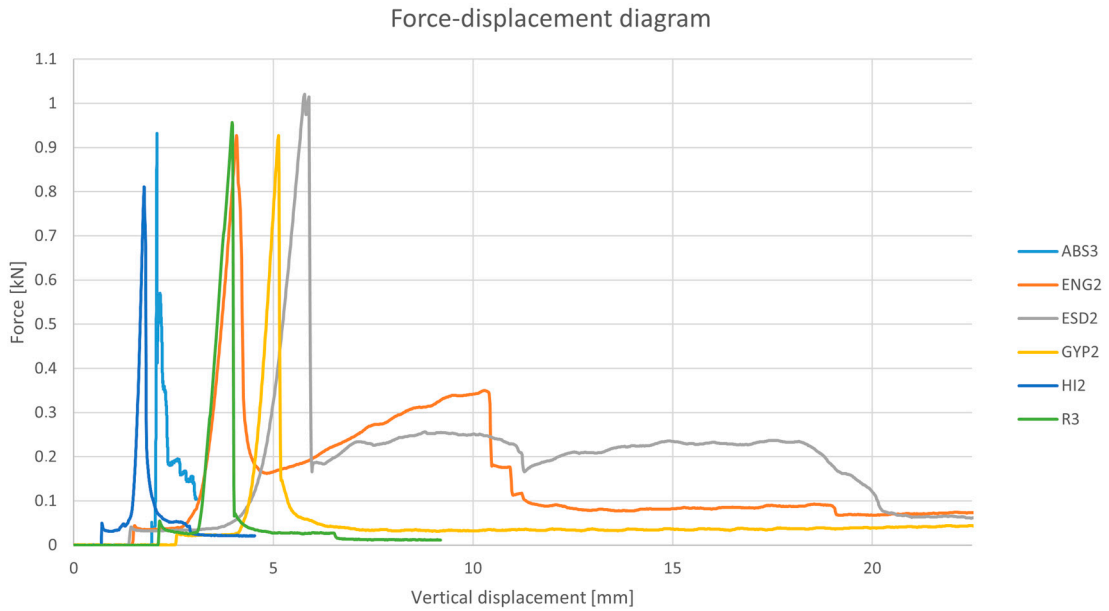

Figure 6. Force–displacement diagram of the specimens (ABS, ENG, ESD, GYP, HI, and R).

All the data in the figure are measured values and maintain a proportional relationship. In this scenario, only the loading speed can be adjusted—either accelerated or decelerated—since the machine applies a constant force of 20 kN.

If the measurement speed were increased, the graph's curves would appear shorter, resulting in fewer vertical displacement values. Conversely, reducing the measurement speed would extend the curves, increasing the number of vertical displacement values.

The maximum values, so that the diagram does not become overcrowded, are been plotted on the diagram; nevertheless, the differences are still clearly visible. The peak values were in the following descending order: ESD, R, ABS, ENG, GYP, and HI. Their peak values were at 1.021, 0.956, 0.933, 0.928, 0.927, and 0.812 kN. As can be seen from the figure, the reinforced specimens showed different behavior during the loading tests.

The staircase-like decreasing structures observed in the results highlight the impact of reinforcement after reaching a peak value, which is particularly noticeable in the ESD, ENG, and ABS specimens. In contrast, this behavior was not evident in the unreinforced (R) specimens or in the GYP and HI specimens. These differences in behavior may be attributed to multiple factors.

Firstly, the variations could be linked to the inherent material properties. Specifically, HI and GYP materials exhibit lower tensile strength compared to ESD, ABS, and ENG, which inherently makes them less effective in maintaining structural integrity under load. Additionally, HI and GYP also possess lower heat resistance, as outlined in Table 2, which could further limit their performance under certain conditions.

Another potential explanation lies in the chemical interactions between the materials and the concrete medium. Such interactions could compromise the structural integrity of the materials, making them less suitable for broader applications. If this hypothesis were to hold true, it would indicate a significant limitation in the usability of these materials for reinforced concrete structures. Consequently, investigating this phenomenon in greater detail is of critical importance to understanding and addressing the observed differences.

Furthermore, as illustrated in Figure 6, no amplification of the reinforcement effect was observed for the GYP and HI specimens. This further supports the notion that their lower

mechanical and thermal performance, combined with possible chemical incompatibility, reduces their effectiveness when used as reinforcing agents. This highlights the necessity for further research to better evaluate the potential of these materials in reinforced concrete applications. In Figure 6, no amplification effect after a peak value is observed in the flattening parts. Specimens R, GYP, and HI exhibited immediate failure, while specimens ESD, ABS, and ENG showed resistance to loading even after fracture (peak value).

This shows the brittle behavior of the inner reinforcement material in GYP and HI, which indicates the chemical dissolution of PLA during the 28-day drying cycle.

Figures 7–9 show the displacement of ABS2 test specimens in the *X* direction during the loading time at 0, 20, and 40 s until a fracture occurred.

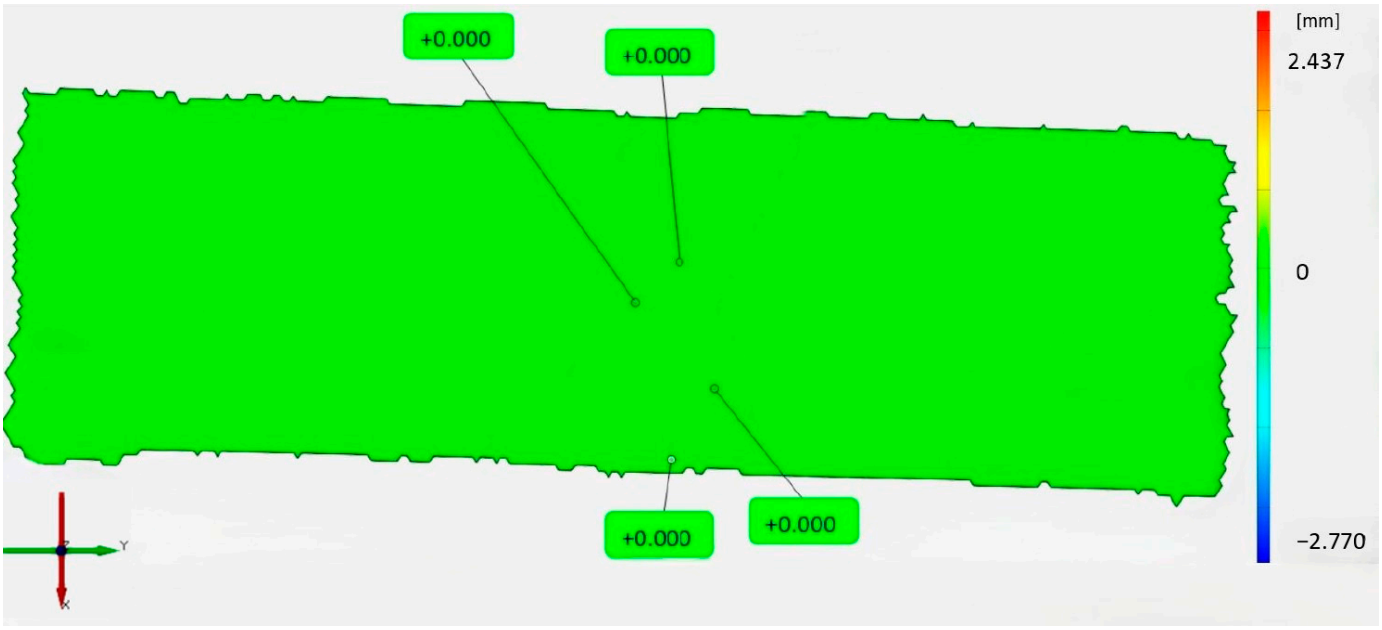

Figure 7. Displacement in *X* direction of ABS2 specimen at 0 s.

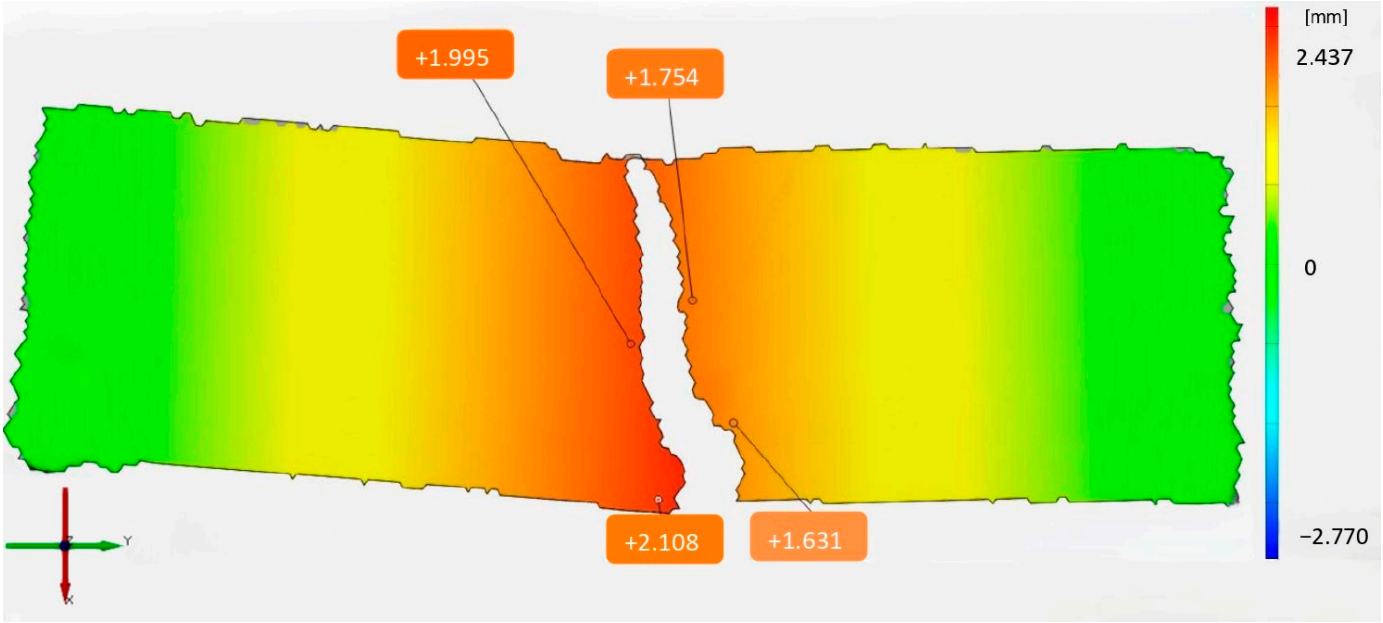

Figure 8. Displacement in *X* direction of ABS2 specimen at 20 s.

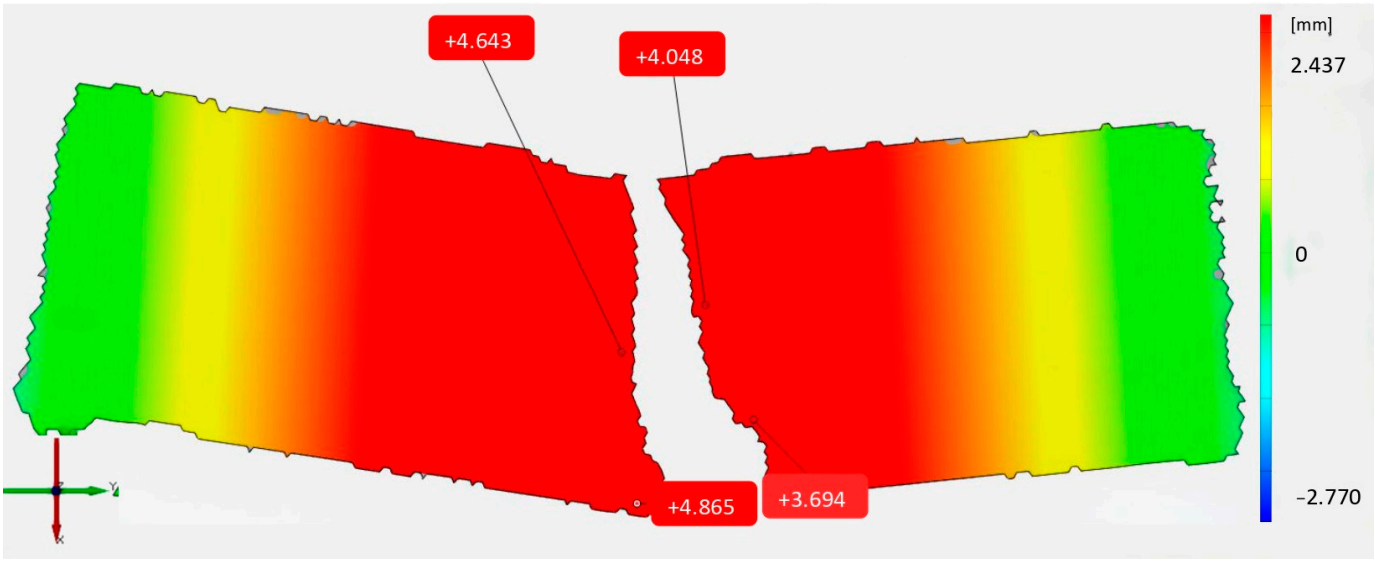

Figure 9. Displacement in *X* direction of ABS2 specimen at 40 s.

Figures 7–9 show the variation over time of the displacements of the selected points (which are in the same position in each figure). In Figure 9, the values are shown in white because the magnitude of their displacement values fell outside the range of the extremes of the scale defined by the statistical calculations.

The extent of the displacements is defined in millimeters, as indicated on the scale. In this case, the scale maximum of +2.437 and the scale minimum of −2.770 are averaged over all the measurements.

The scale values are set to the same value for all DIC measurements so that the measurement results can be compared. The values in Figures 7 and 8 are shown in black because they fell within the defined range.

During the evaluation of the measurement results, when the displacement data in the *X* direction for Figure 6 were collected and evaluated, the maximum displacement value at the bottom of the crack in Figure 9 was linearly interpolated for ABS2, according to the range of the HBM data logger. This method was also used for the other specimens.

After the fracture tests, the internal structure of the PLA became visible. In the GYP test specimens, one of the most noticeable features on the surface of the infill was the absence of PLA in several places and the formation of holes at the joints of the infill.

Figure 10 illustrates the surface of the GYP1 specimen, with white precipitation observed on both sides.

Figure 10. Formation of holes in the GYP material reinforced concrete with white precipitation.

To compare the separation and the difference between the two materials, for example, in the case of the ABS2 specimen, the reinforcing element did not break or tear apart under

load but separated from the surface without adhering to the concrete. Figure 11 illustrates the ABS2 specimen with white precipitation observed within the fractured specimen.

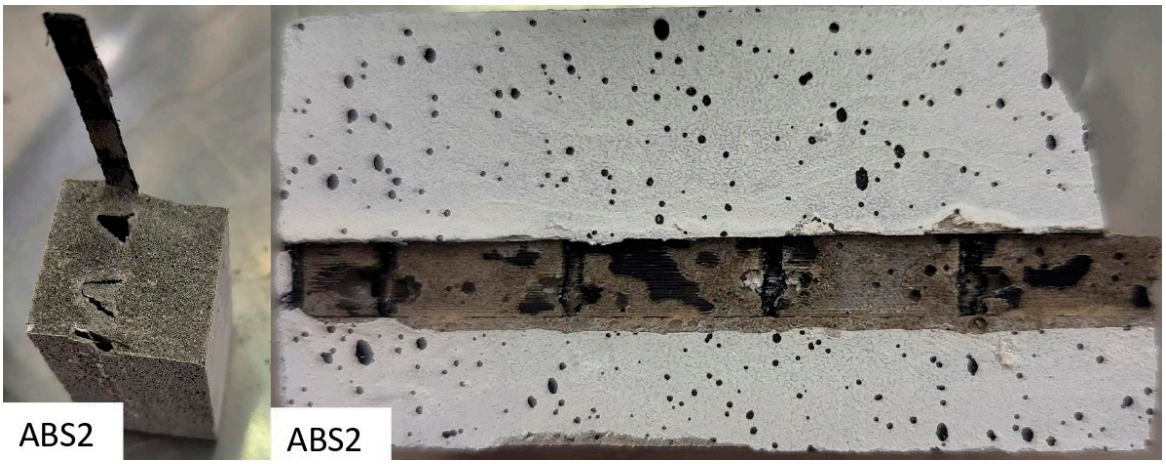

Figure 11. Separation of the ABS reinforcement from the concrete without adhering to white precipitation.

After the bending tests were performed, the broken test specimens were placed back into simple tap water. This step was important for comparing the results of the dissolution tests.

3.1.1. Observations During and After the Casting

After the specimens were stripped from the casting mold, their surfaces were smooth and evenly covered with concrete (cement grout), so painting of the specimens was easily performed. They were then stored in water to ensure their internal drying and good surface quality.

Shrinkage (contraction) measurements were carried out using GOM ATOS Triple Scan, where the shrinkage was determined by comparing the scanned CAD (computer-aided design) models; the results are presented in Section 3.2.

In the current section, the surface changes and observations of the test specimens are presented. During underwater storage, the concrete in most of the specimens, where the layer was thinnest, partially or entirely flaked off, revealing the reinforcing element.

Figure 12 shows the test specimens stored under water for 21 days prior to the DIC measurements (performed by the GOM ATOS instrument), where the reinforcing element is visible due to the flaking.

Figure 12. Surface of concrete specimens before DIC measurements (executed by GOM ATOS and GOM ARAMIS instruments).

The positioning of the reinforcement materials impacts the structural performance and bending behavior of the samples. If the amplification were closer to the neutral axis, it would reduce the amplification effect. On closer inspection of the concrete elements, it was observed that white precipitation occurred, and it was most prominent on the GYP and HI

specimens' surfaces, but minimal signs of precipitation can also be seen on ENG and ESD specimens. Only in the case of ABS specimens was there no precipitation on the surface. The white, powdery precipitate is likely to be lime from the concrete.

Another observation related to Figure 8 is the flaking of the thin concrete layer surrounding the reinforcing element. Initially, the specimens, when placed under water, had a smooth, even surface free of cracks. On the 14th day, tiny visible cracks appeared in the regions where partial flaking occurred by the 21st day. The detachment of the thin concrete layer from the reinforcing layer could have been caused by the white substance that formed as a solid deposit, resembling powder or even the presence of water.

Flaking can damage the surface of the specimens, which could cause errors during the DIC measurement series. The precipitation phenomenon was already observed in the previous publication of the authors of the current paper, where amorphous PLA waste was used as a reinforcing element [66]. Figure 13 shows the white material precipitated on the surfaces of the HI and GYP specimens.

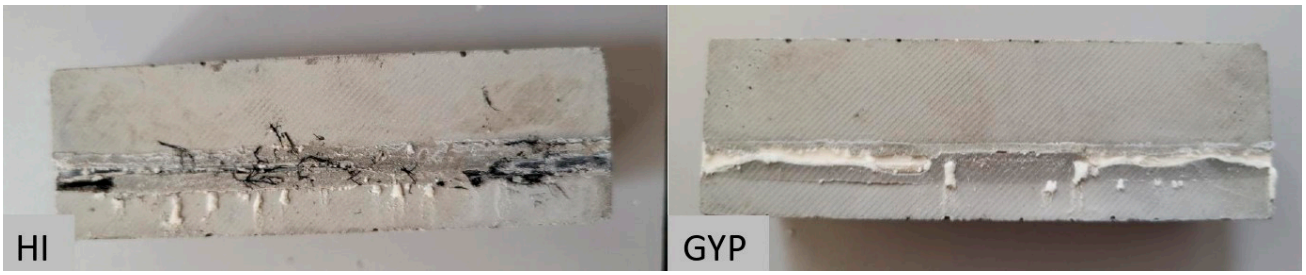

Figure 13. White material precipitated on the surfaces of the HI and GYP specimens.

In the case of HI specimens, it was further observed that the 3D-printed fibers on the longer side of the test specimen started to split and separate from each other layer by layer. This observation foreshadows the possibility of the entire printed structure disintegrating.

3.1.2. Observations During and After Drying of Concrete with GOM ATOS

The specimens were observed with GOM ATOS during and after the drying cycle (28 days) of the concrete structures. Before scanning measurements were started, the specimens were dried for 12 h, as the system is only capable of detecting a matte, gloss-free surface. The test specimens were scanned twice on days 21 and 28 of the drying cycle.

During the underwater treatment of the specimens, the thinnest concrete layer, which coated the reinforcing PLA patterns, partially flaked off, leaving them exposed. Therefore, these surface parts with severe defects were not taken into account during the ATOS scanning measurements, so the extent of their surface deviation was not taken into account. This procedure was used to compare the initial CAD model with the cast test specimen that had been under water for 21 days and to compare the 21-day test condition with the 28-day test condition. Table 5 represents the deviation values of the test specimens.

Table 5. Deviation values of the specimens ("+" means expansion; "−" means shrinkage).

Material	Standard Deviation from CAD Model at Day 21 [mm]	Longitudinal Deviation [%]	Transverse Deviation [%]	Difference Between 21 and 28 Days [mm]	Max Difference [mm]
R	0.1	−0.40	−1.20	±0.01	±0.11
ESD	0.2	−0.20	−1.20	±0.15	±0.35
ABS	0.25	−0.45	−0.40	±0.20	±0.45
ENG	0.1	−0.50	+0.08	±0.20	±0.30
GYP	0.1	−0.37	−0.24	±0.05	±0.15
HI	0.2	−0.37	+0.16	±0.10	±0.30

As summarized in Table 5, the sum of the deviations did not reach 0.5 mm in any of the cases, even though the maximum deviation was only 0.45 mm for the ABS specimens. The deviation values suggest that the specimens shrunk in the longitudinal direction and also shrunk in the transverse direction, excluding ENG and HI specimens. The test specimens were again stored in an underwater medium after the measurement on day 21, and the measurement was repeated on day 28.

At the end of the ATOS measurements, the residue of the flaked concrete covering the reinforcement had to be cleaned off for the GOM ARAMIS measurements. The painted measurement points would have acted as erroneous, incomplete measurement data if they had not been flaked off.

It is important to note that the specimens had to be dried before starting the ARAMIS measurements and the load tests, as the residual moisture content would have affected the measurement results. This was verified by hourly weighing of the specimens after 24 h of drying at room temperature. When the standard deviation of the weight values was minimal, the authors started to execute the ARAMIS measurements.

3.2. Concerning the Dissolution Tests of the PLA Specimens

During the dissolution tests, 3D-printed PLA samples with a thickness of 0.4 mm were immersed in solutions with pH values of 12 and 12.55. Each specimen was submerged in 50 mL of solution, covered, and kept for four weeks (28 days).

Preventing evaporation was key, as it ensured that the pH of the solution remained constant throughout the measurement. The observation was a subjective process; therefore, the evaluations were conducted based on a custom assessment system. During the observations, only the first week of the dissolution tests was observed for a full seven days since the rate of change in the test samples slowed down after the first week. Table 6 summarizes the one-week-long 24 h observations of the dissolution tests on the specimens and contains the list of symbols used.

Table 6. Summary of observations during the dissolution tests with the list of symbols.

Material	Solution pH	Day 1	Day 2	Day 3	Day 4	Day 5	Day 6	Day 7
ESD	12	NC	C	C	C, P	C, I	C, CRP	C, CRP, I
ENG	12	NC	C, P	C, I	C, I	C, I	C, CRP, S	C, CRP, S, I
HI	12	NC	C, P	C, I	C, I	C, I	C, CRP, S	C, CRP, S, I
ABS	12	NC	C, P	C, I	C, I	C, I	C, CRP	C, CRP, I
GYP	12	NC	C, P	C, I	C, I	C, I	C, CRP, S	C, CRP, S, I
ESD	12.55	NC	C	C, P	C, P	C, I	C, I	C, CRP
ENG	12.55	NC	C	C, I	C, I	C, I	C, CRP, S	C, CRP, S, I
HI	12.55	NC	C, P, F	C, F, I	C, F, I	C, F, I	C, F, CRP, S	C, F, CRP, S, I
ABS	12.55	NC	C	C, P	C, I	C, I	C, CRP	C, CRP, I
GYP	12.55	C	C, P	C, I	C, I	C, CRP	C, CRP, S, W	C, CRP, S, W, I

Remarks

The solution does not run off the surface, covering it evenly—C.
The solution runs off the surface, no coverage—NC.
Faded surface where the specimen was in contact with the solution—F.
Small amount of white substance that forms as a solid deposit, resembling powder on the surface—P.
Increase in the amount of precipitation—I.
Precipitation occurred in the solution as tiny particles—S.
Precipitation occurred on the wall of the measuring cup—W.
White crystal-like precipitation in continuous lines, parallel to the printing direction—CRP.

During the 168 h observation period of the dissolution tests, the GYP specimens exhibited the most significant and noticeable changes and reactions to the solution. In the

first 24 h of the test, the solution uniformly coated the surface of the GYP specimens while it rolled off the surface of the other specimens. By the second day, all specimens tested in the pH 12.55 and pH 12 solutions were uniformly coated by the solution.

In the pH 12.55 solution, a small amount of white substance that formed as a solid deposit, resembling powder, was observed on the GYP and HI specimens, whereas in the pH 12 solution, similar precipitation was observed on the ENG, HI, ABS, and GYP specimens. This type of precipitation could occur due to the crystallization of dissolved compounds when the solution became oversaturated, a chemical reaction between solutes, or environmental factors such as changes in temperature or pH. The appearance and composition of this precipitation can vary depending on the specific compounds involved, but it typically consists of solid particles that settle or adhere to surfaces.

Additionally, in the pH 12.55 solution, the black surface of the HI specimens where they contacted the solution had faded to gray. Figure 14 illustrates the fading of the color observed on the surface of the HI specimen in the 12.55 pH solution.

Figure 14. Fading of the color of the HI specimen immersed into the 12.55 pH solution with a small amount of white precipitation on day 7.

On the third day, a small amount of white precipitation appeared on the ESD specimen immersed in the pH 12.55 solution. For all other specimens with pre-existing precipitated particles, the amount of precipitation increased. On the fourth day, the amount of precipitation in all cases further increased; no other significant change was observed.

On the fifth day, the powder-like structure of the precipitation, in the case of GYP immersed in the 12.55 pH solution, turned into a crystal-like structure parallel to the direction of the printing direction of the specimens.

On the sixth day, a crystal-like solution appeared in all cases immersed in the 12 pH solution and all cases immersed in the 12.55 pH solution except the ESD specimen. In the case of ENG, HI, and GYP specimens, precipitation occurred as tiny, floating particles in both solutions; in the case of GYP immersed in the 12.55 pH solution, the precipitation also occurred in the wall of the measuring cup as well as in the solution.

On the seventh day, white crystal-like precipitation occurred in ESD immersed in the 12.55 pH solution. In addition, the amount of precipitation increased in all other test samples and the solutions.

Figure 15 shows the occurrence and the changing of the precipitation during the observation of the dissolution tests.

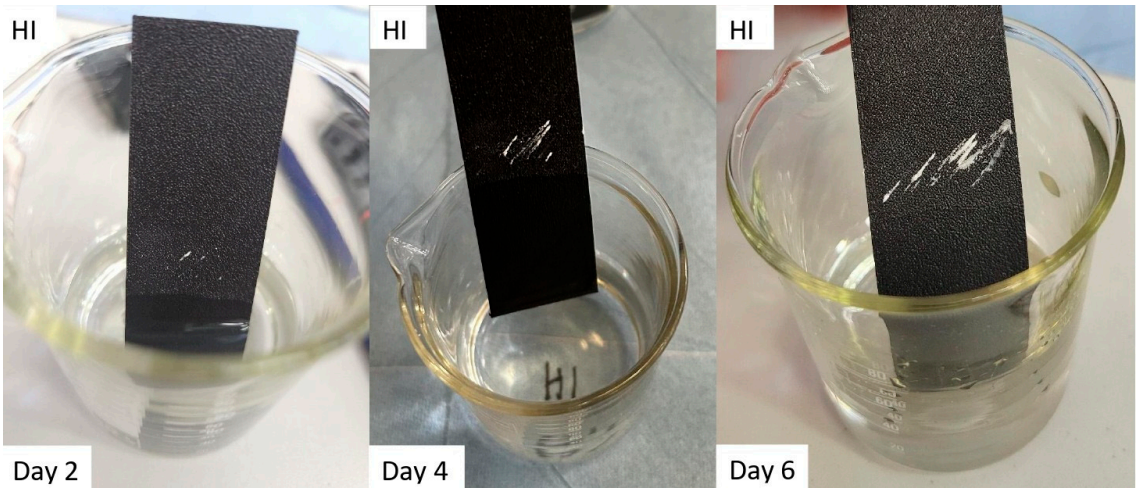

Figure 15. Occurrence of the precipitation by the time observed at the HI specimens.

The remaining time of the dissolution tests was monitored weekly, where changes in the surface of the test specimens and the amount of solution remaining were observed. Despite covering the solution, the amount of the solution decreased. Table 7 shows the percentage reduction in the solutions from the original initial volume of 50 mL, all compared to the previous volume.

Table 7. Decrease in the amount of solution at pH 12.55 and pH 12 during the four-week period.

Material	Week 1	Week 2	Week 3	Week 4
pH 12.55 solutions				
ESD	40	30	25	5
ENG	40	25	25	10
HI	40	35	25	0
ABS	40	30	20	10
GYP	50	25	25	0
Material	**Week 1**	**Week 2**	**Week 3**	**Week 4**
pH 12 solutions				
ESD	20	40	35	5
ENG	20	45	30	5
HI	30	45	25	0
ABS	20	30	35	15
GYP	50	25	25	0

The most significant decrease in solution amount, in percentage terms, was observed in the GYP specimens, where the material absorbed half of the solution in both the 12.55 and 12 pH solutions. Observing Table 7, it can be seen clearly that the next value after the GYP percentage was a decreased value (50%), while 40% was observed for the rest of the solutions with pH 12.55. This was followed by the HI sample of the pH 12 solution with a 30% decrease, followed by the combination of ABS, ESD, and ENG samples with a 20% decrease.

By the second week, the amount of precipitation had noticeably increased, while the amount of solution had decreased in all samples but not to the same extent. In the case of pH 12 solutions, the most significant amount of decrease was in the case of the HI and ENG specimens at 45%, followed by 40% in the case of ESD, then 30% with ABS, and a 25% decrease with GYP. By the third week, both the pH 12 and pH 12.55 solutions ran out of solution from the GYP and HI test samples. By the fourth week, no liquid remained in either solution for HI and GYP, and only the amount of white precipitate increased. In

contrast, at pH 12, 15% of the solution remained for ABS and 5% for ENG and ESD. For the same materials, the liquid was also retained in the pH 12.55 solution: 10% for ABS and ENG and 5% for ESD.

As the solutions slowly ran out in the beakers, the white precipitate-like material on the test samples increased. Figure 16 shows the formation and weekly spread of white substance and on the HI specimen immersed in the pH 12.5 solution.

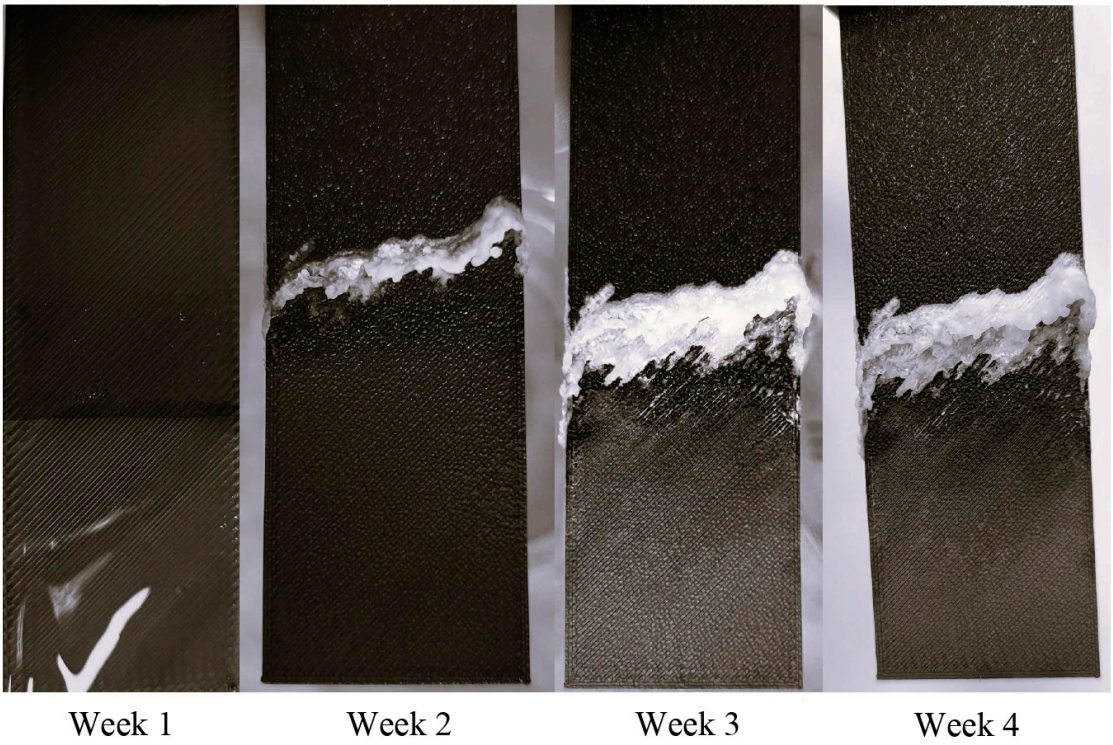

Figure 16. Weekly spread of white substance and fading on ENG specimen in the pH 12.55 solution.

As shown in Figure 16, the white precipitate is widely spread on the surface of the specimen; what is interesting about the location of the white material is that it started to form on the line where the specimen touched the solution, and the HI material started to fade. However, to find out where it came from—whether it came from the reinforcing material or crystallized out of the solute—further experiments were needed. Since one way of detecting NaOH is by combustion, a test was carried out on a sample taken from the surface. If it burned with a yellow flame, it was NaOH; if not, it originated from PLA, and its compound must be determined.

Since the research had limited resources, the simplest and quickest methods were used to determine the substance. Flame tests and dissolution tests were carried out using the same equipment. Table 8 shows the test results of the flame tests and pH measurements of the white precipitate samples tested.

Before starting the experiments, a sample of white material was taken from each of the test samples. All samples were then heated one at a time for the same length of time. Of the samples tested, only the sample from the GYP probe showed a color change in response to heat.

Another simple method for detecting NaOH was to measure pH. Since NaOH is a strong alkali, if it is present, the pH of the solution will be very high (between 12 and 14). The measurements showed that although the pH values were close to 11, none of the solutions reached the very alkaline value. However, during the dissolution tests of the pH 12.55 solution on a sample taken from the ABS specimen, the solution became unclear, and black particles started floating in it.

Table 8. Flame test and pH measurement test results of the white matter.

Material	Reaction to Flame	Dissolution	pH Value	Temperature [°C]
pH 12.55 solutions				
ESD	none	full	10.14	21.0
ENG	none	full	10.31	20.9
HI	none	full	10.39	20.2
ABS	none	uneven	10.62	21.2
GYP	decolorization	uneven	10.81	21.6
Material	**Reaction to flame**	**Dissolution**	**pH Value**	**Temperature [°C]**
pH 12 solutions				
ESD	none	full	10.47	22.5
ENG	none	full	10.66	22.9
HI	none	full	10.17	22.0
ABS	none	uneven	10.19	24.1
GYP	none	full	10.17	23.2

For the sample solution from GYP, black particles appeared, and the solution was decolorized from translucent to slightly yellow. In the pH 12 solution dissolution tests, as well as with a sample from the ABS sample, the sample dissolution was incomplete, and white, floating particles made the solution cloudy. An important note is that in the dissolution tests, the samples were dissolved in water only when heated.

Some specimens containing the white precipitate did not completely dissolve in distilled water, even under heat. pH tests indicated a reaction between the NaOH solution and the PLA-based and ABS materials. If the specimens had been coated solely with pure NaOH (used to simulate the high pH of concrete), they would have burned with a yellow flame in flame tests, and pH levels would have remained around 12 instead of falling below 11. This suggested a chemical interaction between the reinforcement materials and the solution.

3.3. Concerning the Dissolution of the Fiber-Reinforced Concrete Specimens Underwater

The dissolution tests of the reinforcing materials were carried out in parallel with tests on the broken fiber-reinforced concrete specimens stored underwater. The specimens were stored in tap water, covered, and subjected to the three-point bending test for a further 4 weeks after the fracture tests. During this time, the pH and temperature of the aqueous medium were monitored. The pH and temperature of the medium were rechecked after a further 4 weeks, i.e., at week 8 after the start of the observation, to see if there were any outliers. Table 9 represents the pH values and the temperature of the aqueous medium over the four-week study.

Table 9. pH and temperature changes in aqueous medium over four weeks plus one week.

Observed Period in Weeks	pH Value	Temperature [°C]
1st	7.75	21.2
2nd	7.99	21.0
3rd	8.05	21.2
4th	8.19	21.4
8th	8.10	20.8

The measured pH values fell in the alkaline range but were not high enough (9–12) to clearly indicate the presence of calcium hydroxide ($Ca(OH)_2$). The pH increase caused by $Ca(OH)_2$ was generally more significant, as it is a highly alkaline substance.

Rising pH values (7.73 → 8.19) could indicate that a solution is alkalinizing, but other alkaline substances such as carbonates (e.g., sodium carbonate) can also be responsible.

It is also possible that the chemical equilibrium of the solution is altered, for example, by loss of carbon dioxide, which could cause natural alkalinization. This issue needs further investigation.

In the third week of the observations, white crystals, similar to the white material observed in the dissolution tests, appeared on the concrete elements in all cases right next to or on the reinforcing element. The observed white crystalline particles are presented in Figure 17.

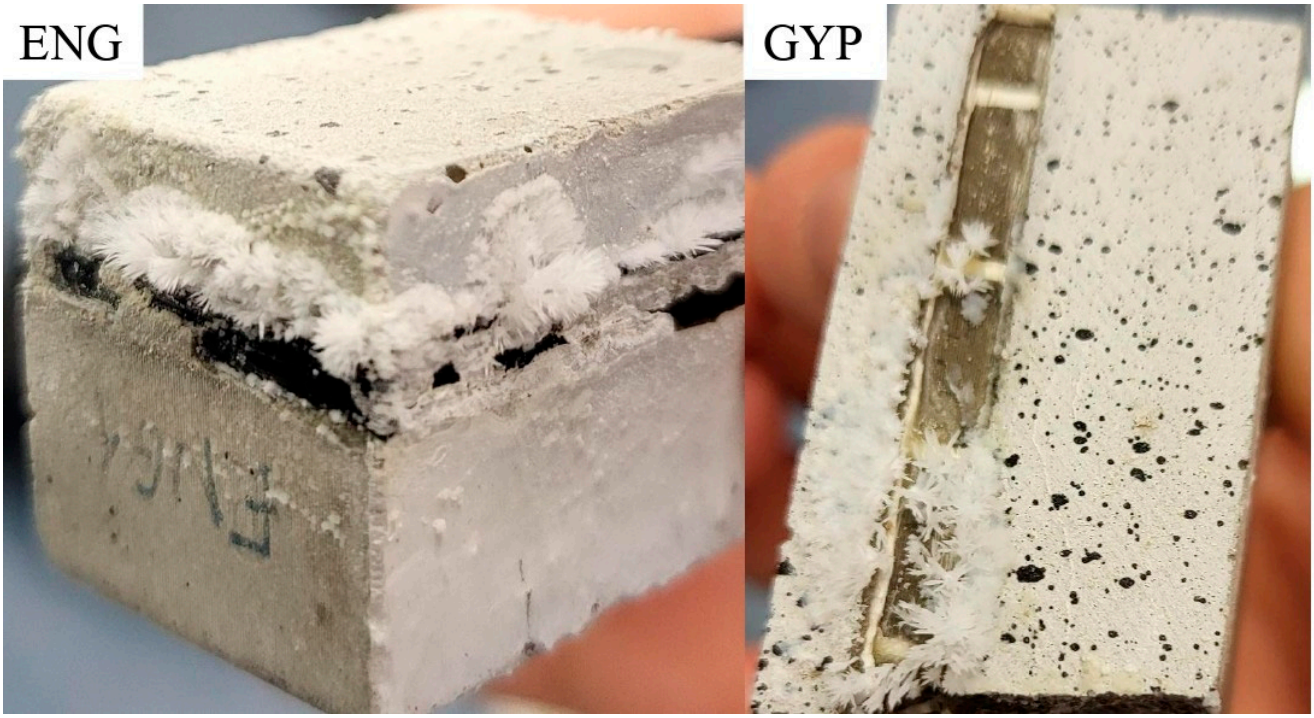

Figure 17. Occurrence of white crystals on the reinforced concrete beams kept underwater for four weeks.

Another observation outside the appearance of crystals was the behavior of PLA-based materials. In several parts, especially HI, the material was exposed to water due to fracture and disintegrated on contact. ENG, GYP, and ESD were smeared.

As shown in Figure 18, HI was the most severely affected by the material condition. While ABS was completely intact compared to the other PLA-based materials, ENG, GYP, and ESD samples were smearable with HI, which even showed fiber degradation.

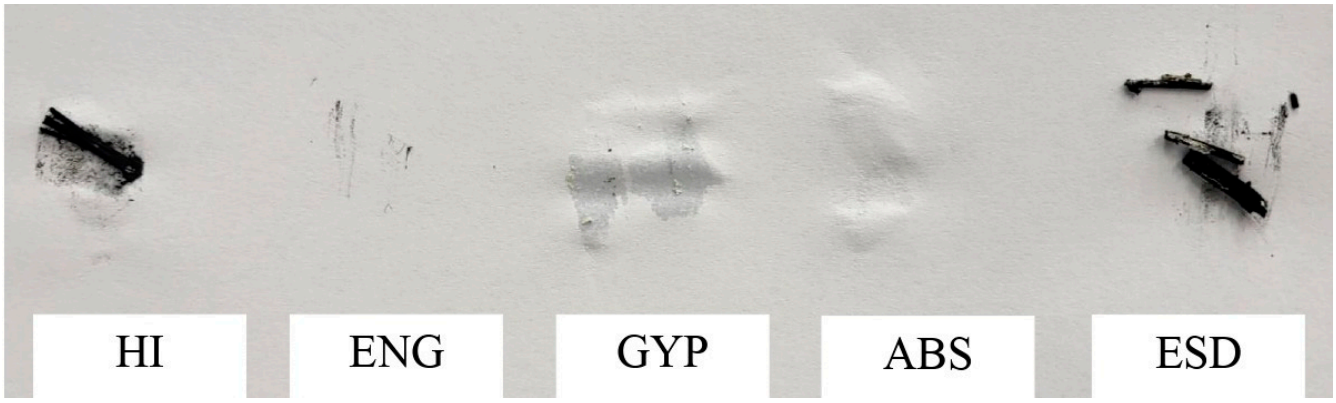

Figure 18. The smearable texture on paper of PLA materials exposed to water in week 3.

These observations were necessary, as only by measuring the pH of the medium in a continuous flow could it be determined whether the white matter released was lime leached from the concrete. Since $Ca(OH)_2$ forms an alkaline solution in water, the pH of the water will be higher than 7. The alkalinity of the solution (pH around 9–12) could be quickly determined by using a pH meter.

As the results of the pH measurements (measured with identical equipment used in the dissolution tests of the PLA and ABS samples) showed, the pH values did not even exceed 8.20, even in the back-tested range, after week 8.

4. Conclusions

This study aimed to evaluate the mechanical performance, chemical stability, and reinforcement potential of 3D-printed materials, including PLA, ABS, and electrical ESD PLA, in concrete and NaOH mediums. The results provided insights into both the strengths and limitations of these materials, paving the way for advancements in sustainable construction. The following conclusions align with the research objectives and summarize the key observations.

The conclusions regarding mechanical performance under load are as follows:

- Unreinforced concrete specimens demonstrated unexpectedly higher load-bearing capacity than reinforced counterparts in specific cases, challenging the assumption of universal reinforcement benefits;
- Electrical ESD PLA emerged as the most promising reinforcement material, exhibiting superior post-failure load-bearing capacity and minimal degradation in high-pH environments;
- Observations under mechanical loading revealed faster and more extensive white precipitate formation in specimens subjected to lower loads, suggesting a connection between load resistance and chemical stability.

The conclusions regarding chemical stability in NaOH and concrete mediums are as follows:

- Dissolution tests confirmed that the white substance that formed as a solid deposit, resembling powder, originated from chemical reactions involving PLA-based materials in high-pH environments rather than from lime in the concrete;
- PLA and ABS materials showed susceptibility to slow degradation in NaOH solutions, leading to reduced long-term structural stability;
- pH measurements indicated that NaOH interacted chemically with PLA-based and ABS materials, further emphasizing the need for reinforcement materials resistant to high-pH degradation.

The conclusions regarding the evaluation of diverse materials for reinforcement potential are as follows:

- Electrical ESD PLA demonstrated high chemical stability and strong mechanical performance, making it a viable candidate for sustainable construction applications;
- Alternative materials like PET-G and PCTG, along with surface treatments, were identified as potential solutions to mitigate the drawbacks of PLA-based reinforcements while retaining their benefits.

The limitations identified in this research highlight the challenges of using PLA materials for reinforced concrete applications. PLA's inherent thermal and hydrolytic instability, combined with its thermal expansion mismatch with traditional construction materials, restricts its long-term durability. Additionally, its vulnerability to degradation in alkaline environments further complicates its use in demanding applications, such as bridges or outdoor concrete structures exposed to moisture and temperature fluctuations. While combining PLA with other materials has shown a potential to mitigate some of these issues,

further research is essential to fully address these limitations. Advancing material optimization and exploring the chemical interactions between PLA and concrete will be critical for realizing PLA's potential as a sustainable and reliable alternative for reinforcement.

ABS filaments were chosen as the reference material in this study because of their established use in engineering and 3D printing, where their high impact resistance, stiffness, and recyclability make them a reliable standard for comparison. PLA filaments, in contrast, were examined as a more environmentally friendly option, offering advantages in printability and reduced ecological footprint. The goal was to assess whether PLA, despite its challenges with thermal and hydrolytic stability, could meet the mechanical and chemical requirements for reinforcing concrete. By evaluating PLA against ABS, the study aimed to identify materials that could combine sustainability with the performance needed for structural applications.

Future research should focus on addressing the chemical stability challenges observed in PLA and ABS materials to enhance their long-term applicability in reinforced concrete structures. Advanced analytical techniques should be utilized to determine the exact chemical composition of the white precipitate and to understand the degradation mechanisms of these materials in high-pH environments. Such studies would provide critical insights into preventing chemical interactions that compromise structural integrity, possibly applying artificial intelligence or learning algorithms [16,76,77], optimization techniques [58,78], further field tests and laboratory examinations [79,80], etc.

Additionally, exploring alternative materials such as PET-G and PCTG offers significant potential. These materials may retain the mechanical and environmental advantages of PLA while offering improved chemical resistance. Surface treatments or coatings for 3D-printed reinforcement materials could further mitigate degradation risks and enhance durability in harsh environments.

In conclusion, this study provides valuable insights into the potential of 3D-printed PLA reinforcement in sustainable construction. While highlighting both its promise and limitations, it lays a foundation for future innovations in material science and concrete engineering.

Author Contributions: Conceptualization, H.C., S.S., D.K., M.S. and S.F.; methodology, H.C., S.S., D.K., M.S. and S.F.; software, H.C., S.S., D.K., M.S. and S.F.; validation, H.C., S.S., D.K., M.S. and S.F.; formal analysis, H.C., S.S., D.K., M.S. and S.F.; investigation, H.C., S.S., D.K., M.S. and S.F.; resources, H.C., S.S., D.K., M.S. and S.F.; data curation, H.C., S.S., D.K., M.S. and S.F.; writing—original draft preparation, H.C., S.S., D.K., M.S. and S.F.; writing—review and editing, H.C., S.S., D.K., M.S. and S.F.; visualization, H.C., S.S., D.K., M.S. and S.F.; supervision, H.C., S.S., D.K., M.S. and S.F.; project administration, H.C., S.S., D.K., M.S. and S.F.; funding acquisition, H.C., S.S., D.K., M.S. and S.F. All authors have read and agreed to the published version of the manuscript.

Funding: This research received no external funding.

Institutional Review Board Statement: Not applicable.

Informed Consent Statement: Not applicable.

Data Availability Statement: The original contributions presented in this study are included in the article. Further inquiries can be directed to the corresponding author.

Acknowledgments: This paper was written by the research team "SZE-RAIL". The authors are thankful for the technical support of Gusztáv Baranyai and Attila Nagy from the Széchenyi István University, Győr, Hungary.

Conflicts of Interest: The authors declare no conflicts of interest.

List of Abbreviations

ABS	Acrylonitrile butadiene styrene
CFRP	Carbon fiber-reinforced polymer
$Ca(OH)_2$	Calcium hydroxide
CO	Carbon monoxide
CO_2	Carbon dioxide
CTB	Cement-based tail backfill
DIC	Digital image correlation
ENG	Engineering PLA
ESD	Electrostatic discharge PLA
GYP	Gypsum PLA
HI	High-impact PLA
NaOH	Sodium hydroxide
OH^-	Hydroxide ion
PBS	Phosphate-buffered saline
PCL	Polycaprolactone
PCTG	Polycyclo-hexylenedimethylene terephthalate glycol-modified
PET	Polyethylene terephthalate
PET-G or PETG	Polyethylene terephthalate glycol-modified
pH	Potential of hydrogen
PLA	Polylactic acid
PP	Polypropylene
SF	Short steel fiber-sprayed epoxy
THF	Tetrahydrofuran
VOC	Volatile organic compound
List of Symbols	
d	Cross-sectional dimension of the concrete specimen according to [67,69]
L	Length of the concrete specimen according to [67,69]
m_x	Quantity of the considered liquid/material in the solution [mol] in the x-th case
n_y	Quantity of the considered liquid/material in the solution [g] in the y-th case

References

1. Kuchak, A.T.J.; Marinkovic, D.; Zehn, M. Finite Element Model Updating—Case Study of a Rail Damper. *Struct. Eng. Mech.* **2020**, *73*, 27–35. [CrossRef]
2. Alsirawan, R.; Koch, E. Dynamic Analysis of Geosynthetic-reinforced Pile-supported Embankment for a High-Speed Rail. *Acta Polytech. Hung.* **2024**, *1*, 31–50. [CrossRef]
3. Koch, E.; Ray, R.P. Impact Assessment of Railway Bridge Construction Schedule, based on 3D Geotechnical Finite Element Modeling. *Acta Polytech. Hung.* **2024**, *1*, 187–205. [CrossRef]
4. Kampczyk, A. Technical specifications for interoperability and the provisions of Polish design geometry of the railway line. *Bauingenieur* **2015**, *90*, 229–234. [CrossRef]
5. Kampczyk, A.; Rombalska, K. Configuration of the geometric state of railway tracks in the sustainability development of electrified traction systems. *Sensors* **2023**, *23*, 2817. [CrossRef]
6. Singh, T.; Patnaik, A.; Ranakoti, L.; Dogossy, G.; Lendvai, L. Thermal and sliding wear properties of wood waste-filled poly (lactic acid) biocomposites. *Polymers* **2022**, *14*, 2230. [CrossRef]
7. Dogossy, G.; Morauszki, T.; Ronkay, F. Experimental investigation and applicability of multi-stage simulations in the case of a thick-walled injection-moulded composite. *Appl. Sci.* **2022**, *12*, 8415. [CrossRef]
8. Dižo, J.; Blatnický, M.; Sága, M.; Harušinec, J.; Gerlici, J.; Legutko, S. Development of a new system for attaching the wheels of the front axle in the cross-country vehicle. *Symmetry* **2020**, *12*, 1156. [CrossRef]
9. Dižo, J.; Blatnický, M.; Harušinec, J.; Suchánek, A. Assessment of dynamics of a rail vehicle in terms of running properties while moving on a real track model. *Symmetry* **2022**, *14*, 536. [CrossRef]
10. Kocsis Szürke, S.; Saly, G.; Lakatos, I. Analyzing Energy Efficiency and Battery Supervision in Electric Bus Integration for Improved Urban Transport Sustainability. *Sustainability* **2024**, *16*, 8182. [CrossRef]

11. Kocsis Szürke, S.; Sütheö, G.; Őri, P.; Lakatos, I. Self-Diagnostic Opportunities for Battery Systems in Electric and Hybrid Vehicles. *Machines* **2024**, *12*, 324. [CrossRef]
12. Sága, M.; Blatnický, M.; Vaško, M.; Dižo, J.; Kopas, P.; Gerlici, J. Experimental determination of the manson−coffin curves for an original unconventional vehicle frame. *Materials* **2020**, *13*, 4675. [CrossRef] [PubMed]
13. Blatnický, M.; Sága, M.; Dižo, J.; Bruna, M. Application of light metal alloy EN AW 6063 to vehicle frame construction with an innovated steering mechanism. *Materials* **2020**, *13*, 817. [CrossRef] [PubMed]
14. Volkov, V.; Taran, I.; Volkova, T.; Pavlenko, O.; Berezhnaja, N. Determining the Efficient Management System for a Specialized Transport Enterprise. *Nauk. Visnyk Natsionalnoho Hirnychoho Universytetu* **2020**, *2020*, 185–191. [CrossRef]
15. Saukenova, I.; Oliskevych, M.; Taran, I.; Toktamyssova, A.; Aliakbarkyzy, D.; Pelo, R. Optimization of Schedules for Early Garbage Collection and Disposal in the Megapolis. *East.-Eur. J. Enterp. Technol.* **2022**, *1*, 13–23. [CrossRef]
16. Ficzere, P. The Role of Artificial Intelligence in the Development of Rail Transport. *Cogn. Sustain.* **2023**, *2*, 81. [CrossRef]
17. Zöldy, M.; Baranyi, P. The Cognitive Mobility Concept. *Infocommun. J. A Publ. Sci. Assoc. Infocommun. (HTE)* **2023**, 35–40. [CrossRef]
18. Zalacko, R.; Zöldy, M.; Simongáti, G. Comparative Study of Two Simple Marine Engine BSFC Estimation Methods. *Brodogr. Int. J. Nav. Archit. Ocean. Eng. Res. Dev.* **2020**, *71*, 13–25. [CrossRef]
19. Zöldy, M.; Baranyi, P.; Török, Á. Trends in Cognitive Mobility in 2022. *Acta Polytech. Hung.* **2024**, *21*, 189–202. [CrossRef]
20. Zöldy, M.; Zsombók, I. Influence of External Environmental Factors on Range Estimation of Autonomous Hybrid Vehicles. *Syst. Saf. Hum.-Tech. Facil.-Environ.* **2019**, *1*, 472–480. [CrossRef]
21. Buruzs, A.; Kozma, K. The Realization of a Circular Economy in the Construction Industry and Its Adaptation to EU Standards in Hungary. *Chem. Eng. Trans.* **2023**, *107*, 535–540. [CrossRef]
22. Kof-Kiss, D.; Kozma, K. Extraction System Efficiency Assessment Based on Workplace Airspace and Emissions Measurements. *Chem. Eng. Trans.* **2024**, *114*, 757–762. [CrossRef]
23. Szennay, A.; Major, Z.; Horváth, R.; Czédli, H.; Szigeti, C. Providing Decent, Affordable, and Sustainable Housing: Analysing Environmental Impacts of Family Houses Built with Conventional and Unconventional Building Materials. In *Energy Footprint and Sustainability: Case Studies*; Springer Nature: Cham, Switzerland, 2024; pp. 105–126. [CrossRef]
24. Major, Z.; Szigeti, C.; Czédli, H.M. "Green" Tram Tracks for the Sustainability of the Urban Environment. *Chem. Eng. Trans.* **2023**, *107*, 289–294. [CrossRef]
25. Bai, J. Fiber-Reinforced Polymer Types and Properties. In *Advanced Fiber-Reinforced Polymer (FRP) Composites for Structural Applications*; Woodhead Publishing: Cambridge, UK, 2023; pp. 93–99. [CrossRef]
26. Bai, J. (Ed.) *Advanced Fiber-Reinforced Polymer (FRP) Composites for Structural Applications*; Elsevier: Cambridge, UK, 2023; pp. 1–826, ISBN 9780128203460. [CrossRef]
27. United Nations. *Sustainable Development Goals*; United Nations: New York, NY, USA, 2015. Available online: https://sdgs.un.org/goals (accessed on 9 January 2025).
28. Du, G.; Qian, Y. Bio-Inspired Innovations in 3D Concrete Printing: Structures, Materials and Applications. *Appl. Mater. Today* **2024**, *41*, 102459. [CrossRef]
29. Joralmon, D.; Tang, T.; Prakash, S.R.; Verma, H.; Kim, S.; Li, X. Continuous 3D Printing of Metal Structures Using Ultrafast Mask Video Projection Initiated Vat Photopolymerization. *Addit. Manuf.* **2024**, *89*, 104314. [CrossRef]
30. Szívós, B.F.; Szalai, S.; Fischer, S. Deformation Test of 3D Printed Battery Case Using DIC Technology. In Proceedings of the 2023 3rd International Conference on Electrical, Computer, Communications and Mechatronics Engineering (ICECCME), Tenerife, Canary Islands, Spain, 19–21 July 2023; IEEE: Piscataway, NJ, USA, 2023; p. 10253004. [CrossRef]
31. Liparoti, S.; Pantani, R. 3D Printing of PLA-Based Materials. In *Reference Module in Materials Science and Materials Engineering*; Elsevier: Amsterdam, The Netherlands, 2024. [CrossRef]
32. Perarnau Ollé, E.; Farré-Lladós, J.; Casals-Terré, J.; López Martínez, J.A. Enhanced Selectivity of a 3D-Printed Microfluidic Gas Detector towards Different Volatile Organic Compounds (VOCs) for the Effective Monitoring of Indoor Air Quality in Vehicles. *Environ. Technol. Innov.* **2024**, *33*, 103481. [CrossRef]
33. Gerges, T.; Semet, V.; Lombard, P.; Allard, B.; Cabrera, M. Rapid 3D-Plastronics Prototyping by Selective Metallization of 3D Printed Parts. *Addit. Manuf.* **2023**, *73*, 103673. [CrossRef]
34. Milićević, I.; Popović, M.; Dučić, N.; Vujičić, V.; Stepanić, P.; Marinković, D.; Ćosić, Ž. Improving the Mechanical Characteristics of the 3D Printing Objects Using Hybrid Machine Learning Approach. *Facta Univ. Ser. Mech. Eng.* 2022, *online first*. [CrossRef]
35. Abdul Azam, F.'A.; Tharazi, I.; Bakar Sulong, A.; Che Omar, R.; Muhamad, N. Mechanical Durability and Degradation Characteristics of Long Kenaf-Reinforced PLA Composites Fabricated Using an Eco-Friendly Method. *Eng. Sci. Technol. Int. J.* **2024**, *57*, 101820. [CrossRef]
36. Duarte, C.T.; de Queiroz, H.F.M.; Neto, J.S.S.; Cavalcanti, D.K.K.; Banea, M.D. Evaluation of Durability of 3D-Printed Multi-Material Parts for Potential Applications in Structures Exposed to Marine Environments. *Procedia Struct. Integr.* **2024**, *53*, 299–308. [CrossRef]

37. Lara-Topete, G.O.; Castanier-Rivas, J.D.; Gradilla-Hernández, M.S.; González-López, M.E. Life Cycle Assessment of Agave Bagasse Management Strategies: PLA Biocomposites versus Conventional Waste Disposal Practices. *Sustain. Chem. Pharm.* **2024**, *37*, 101435. [CrossRef]
38. Pinlova, B.; Sudheshwar, A.; Vogel, K.; Malinverno, N.; Hischier, R.; Som, C. What Can We Learn about the Climate Change Impacts of Polylactic Acid from a Review and Meta-Analysis of Lifecycle Assessment Studies? *Sustain. Prod. Consum.* **2024**, *48*, 396–406. [CrossRef]
39. Yao, L.; Li, Y.; Li, Y.; Wang, Y.; Wang, L.; Qiu, D.; Weng, Y. Surface Modification of Polylactide Films and Their Hydrolytic Degradation Performances in Artificial Seawater. *J. Appl. Polym. Sci.* **2024**, *141*, e55999. [CrossRef]
40. Jubinville, D.; Tzoganakis, C.; Mekonnen, T.H. Recycled PLA—Wood Flour Based Biocomposites: Effect of Wood Flour Surface Modification, PLA Recycling, and Maleation. *Constr. Build. Mater.* **2022**, *352*, 129026. [CrossRef]
41. Ferdinánd, M.; Várdai, R.; Móczó, J.; Pukánszky, B. A Novel Approach to the Impact Modification of PLA. *Eng. Fract. Mech.* **2023**, *277*, 108950. [CrossRef]
42. Salami, B.A.; Bahraq, A.A.; ul Haq, M.M.; Ojelade, O.A.; Taiwo, R.; Wahab, S.; Adewumi, A.A.; Ibrahim, M. Polymer-Enhanced Concrete: A Comprehensive Review of Innovations and Pathways for Resilient and Sustainable Materials. *Next Mater.* **2024**, *4*, 100225. [CrossRef]
43. van der Zee, M.; Zijlstra, M.; Kuijpers, L.J.; Hilhorst, M.; Molenveld, K.; Post, W. The Effect of Biodegradable Polymer Blending on the Disintegration Rate of PHBV, PBS and PLA in Soil. *Polym. Test.* **2024**, *140*, 108601. [CrossRef]
44. Woo, S.-H.; Wee, J.-W. Characterization of Accelerated Hydrolysis Degradation of Poly (Lactic Acid) in Phosphate Buffered Saline Solution. *Polym. Degrad. Stab.* **2024**, *223*, 110726. [CrossRef]
45. Yildizel, S.A.; Acik, M.; Kaplan, G.; Bayraktar, O.Y. Enhancing Foam Concrete: A Comparative Analysis of PLA+ Fiber Reinforcements with Plain, Hooked, and Corrugated Fibers. *Constr. Build. Mater.* **2024**, *443*, 137807. [CrossRef]
46. Li, Y.; Min, J.; Zhang, J.; Luo, M.; Wang, T.; Fu, Q.; Zhang, J. Enhancing the Stereocomplex Crystallization of PLLA/PDLA Symmetric Blend by Controlling the Degree of Molecular Chain Entanglement. *Polymer* **2024**, *313*, 127740. [CrossRef]
47. Lee, S.; Wee, J.-W. Effect of Temperature and Relative Humidity on Hydrolytic Degradation of Additively Manufactured PLA: Characterization and Artificial Neural Network Modeling. *Polym. Degrad. Stab.* **2024**, *230*, 111055. [CrossRef]
48. Dias, S.; Almeida, J.; Tadeu, A.; de Brito, J. Alternative Concrete Aggregates—Review of Physical and Mechanical Properties and Successful Applications. *Cem. Concr. Compos.* **2024**, *152*, 105663. [CrossRef]
49. Guo, R.; Ou, C.; Ma, L.; Long, Z.; Xu, F.; Yin, C. Experimental Study on Impact Performance of Seawater Sea-Sand Concrete with Recycled Aggregates. *Sustain. Mater. Technol.* **2024**, *41*, e01060. [CrossRef]
50. Ézsiás, L.; Tompa, R.; Fischer, S. Investigation of the Possible Correlations between Specific Characteristics of Crushed Stone Aggregates. *Spectr. Mech. Eng. Oper. Res.* **2024**, *1*, 10–26. [CrossRef]
51. Wu, M.; Yuan, F.; Wang, P.; Li, W. Concentrically Loaded Concrete Columns Reinforced with Steel-FRP Composite Bars (SFCB) and Carbon Fibre-Reinforced Polymer Mesh Fabric (CFRP-MF) Stirrups. *Structures* **2024**, *66*, 106794. [CrossRef]
52. Yu, Y.; Zhou, L.; Liao, Z.; Zheng, Y. Tension Stiffening and Cracking Behaviors in Glass Fiber Reinforced Polymer Bar Enhanced Precast Recycled Aggregate Concrete Specimen. *Structures* **2024**, *69*, 107395. [CrossRef]
53. Tang, C.; Liu, J.; Hao, W.; Wei, Y. Flexural Properties of 3D Printed Graded Lattice Reinforced Cementitious Composites Using Digital Image Correlation. *Mater. Des.* **2023**, *227*, 111734. [CrossRef]
54. Németh, A.; Ibrahim, S.K.; Movahedi Rad, M.; Szalai, S.; Major, Z.; Kocsis Szürke, S.; Jóvér, V.; Sysyn, M.; Kurhan, D.; Harrach, D.; et al. Laboratory and Numerical Investigation of Pre-Tensioned Reinforced Concrete Railway Sleepers Combined with Plastic Fiber Reinforcement. *Polymers* **2024**, *16*, 1498. [CrossRef]
55. Yeganeh, A.E.; Hossain, K.M.A. Structural Behavior of Shear Deficient High Performance Reinforced Concrete Exterior Joints under Bending. *Structures* **2023**, *48*, 1707–1721. [CrossRef]
56. Kuchak, A.J.T.; Marinkovic, D.; Zehn, M. Parametric Investigation of a Rail Damper Design Based on a Lab-Scaled Model. *J. Vib. Eng. Technol.* **2021**, *9*, 51–60. [CrossRef]
57. Singh, H.; Ambekar, R.S.; Das, D.; Danam, V.A.; Katiyar, N.K.; Kanti Das, B.; Tiwary, C.S.; Bhattacharya, J. Enhancing Structural Resilience by Using 3D Printed Complex Polymer Reinforcement for High Damage Tolerant Structures. *Constr. Build. Mater.* **2024**, *425*, 136085. [CrossRef]
58. Fischer, S.; Kocsis Szürke, S. Detection Process of Energy Loss in Electric Railway Vehicles. *Facta Univ. Ser. Mech. Eng.* **2023**, *21*, 081. [CrossRef]
59. Fischer, S. Investigation of the Settlement Behavior of Ballasted Railway Tracks Due to Dynamic Loading. *Spectr. Mech. Eng. Oper. Res.* **2025**, *2*, 24–46. [CrossRef]
60. Nyathi, M.; Bai, J.; Wilson, I. Deep Learning for Concrete Crack Detection and Measurement. *Metrology* **2024**, *4*, 66–81. [CrossRef]
61. Yaya, N.S.; Cao, S.; Yilmaz, E. Effect of 3D Printed Skeleton Shapes on Strength Behavior, Stress Evolution and Microstructural Response of Cement-Based Tailings Backfills. *Constr. Build. Mater.* **2024**, *432*, 136699. [CrossRef]

62. Hematibahar, M.; Milani, A.; Fediuk, R.; Amran, M.; Bakhtiary, A.; Kharun, M.; Mousavi, M.S. Optimization of 3D-Printed Reinforced Concrete Beams with Four Types of Reinforced Patterns and Different Distances. *Eng. Fail. Anal.* **2025**, *168*, 109096. [CrossRef]
63. Stähli, P.; Custer, R.; van Mier, J.G.M. On Flow Properties, Fibre Distribution, Fibre Orientation and Flexural Behaviour of FRC. *Mater. Struct.* **2008**, *41*, 189–196. [CrossRef]
64. Wu, H.; Shen, A.; Cheng, Q.; Cai, Y.; Ren, G.; Pan, H.; Deng, S. A Review of Recent Developments in Application of Plant Fibers as Reinforcements in Concrete. *J. Clean. Prod.* **2023**, *419*, 138265. [CrossRef]
65. Xu, Y.; Wan, Z.; Šavija, B. Elevating Mechanical Performance of Cementitious Composites with Surface-Modified 3D-Printed Polymeric Reinforcements. *Dev. Built Environ.* **2024**, *19*, 100522. [CrossRef]
66. Csótár, H.; Baranyai, G.; Szalai, S.; Fischer, S. Sustainable Uses of 3D Printing Applied to Concrete Structures. *Eng. Proc.* **2024**, *79*, 55. [CrossRef]
67. *MSZ EN 12390-1:2021*; Testing Hardened Concrete. Part 1: Shape, Dimensions and Other Requirements for Specimens and Moulds. European Committee for Standardization: Brussels, Belgium, 2021.
68. *MSZ EN 12390-2:2019*; Testing Hardened Concrete. Part 2: Making and Curing Specimens for Strength Tests. European Committee for Standardization: Brussels, Belgium, 2019.
69. *MSZ EN 12390-5:2019*; Testing Hardened Concrete. Part 5: Flexural Strength of Test Specimens. European Committee for Standardization: Brussels, Belgium, 2019.
70. Reu, P. Speckles and Their Relationship to the Digital Camera. *Exp. Tech.* **2014**, *38*, 1–2. [CrossRef]
71. Reu, P. All about Speckles: Contrast. *Exp. Tech.* **2015**, *39*, 1–2. [CrossRef]
72. Szalai, S.; Szívós, B.F.; Kocsis, D.; Sysyn, M.; Liu, J.; Fischer, S. The Application of DIC in Criminology Analysis Procedures to Measure Skin Deformation. *J. Appl. Comput. Mech.* **2024**, *10*, 817–829. [CrossRef]
73. Szalai, S.; Szürke, S.K.; Harangozó, D.; Fischer, S. Investigation of Deformations of a Lithium Polymer Cell Using the Digital Image Correlation Method (DICM). *Rep. Mech. Eng.* **2022**, *3*, 206–224. [CrossRef]
74. Grubb, J.A.; Lura, H.S.; Kakad, A.M. *Concrete International*; American Concrete Institute (ACI): Detroit, MI, USA, 2007; pp. 78–83.
75. *MSZ ISO 3696:1992*; Water for Analytical Laboratory Use. Specification and Test Methods. Hungarian Standards Institution: Budapest, Hungary, 1992.
76. Zamfirache, I.A.; Precup, R.E.; Petriu, E.M. Q-Learning, Policy Iteration and Actor-Critic Reinforcement Learning Combined with Metaheuristic Algorithms in Servo System Control. *Facta Univ. Ser. Mech. Eng.* **2023**, *21*, 615–630. [CrossRef]
77. Nosonovsky, M.; Aglikov, A.S. Triboinformatics: Machine Learning Methods for Frictional Instabilities. *Facta Univ. Ser. Mech. Eng.* **2024**, *22*, 423–433. [CrossRef]
78. Mzili, T.; Mzili, I.; Riffi, M.E.; Pamucar, D.; Simic, V.; Kurdi, M. A novel discrete rat swarm optimization algorithm for the quadratic assignment problem. *Facta Univ. Ser. Mech. Eng.* **2023**, *21*, 529–552. [CrossRef]
79. Zheng, J.; Wang, L. Experimental study on creep loading of porous coal under different influencing factors. *Facta Univ. Ser. Mech. Eng.* **2024**, *22*, 153–163. [CrossRef]
80. Liović, D.; Franulović, M.; Ferlič, L.; Gubeljak, N. Surface roughness of Ti6Al4V alloy produced by laser powder bed fusion. *Facta Univ. Ser. Mech. Eng.* **2024**, *22*, 63–76. [CrossRef]